acetate and cobalt acetylacetonate which could result in very small cobalt particles and stronger metal-support interaction showed a large portion of Co species that was reduced at higher reduction temperature. Any Co not reducible during the H_2 reduction up to 800°C is identified as "non-reducible" Co silicate [15,16]. However, for a given Co precursor, Co/SiO_2 and Co/MCM-41 exhibited similar TPR profiles. The results suggest that pore structure of the supports (SiO_2 or MCM-41) has little influence on the metal-support interaction on silica supported Co catalysts.

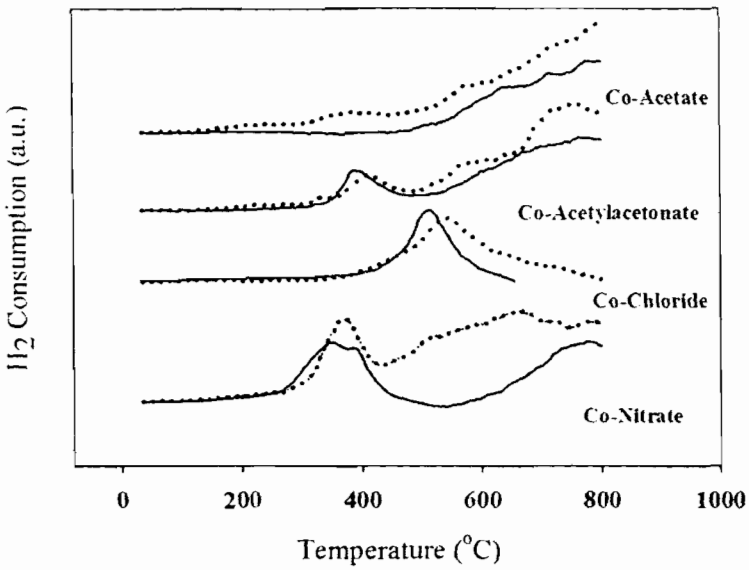

Fig. 2. Temperature program reduction (TPR) profiles of Co/MCM-41 (·····) and Co/SiO_2 (———).

The results of CO hydrogenation reaction test are reported in Table 2. It was found that Co-/M-NO exhibited the highest CO hydrogenation rate than all other catalysts in this study. The higher activity of such catalyst reflects the relatively high dispersion of cobalt on the catalysts. The catalysts prepared from cobalt chloride showed very low activities due to their low Co dispersion and maybe residual Cl^- blocking Co active sites [10]. The low activities of the ones prepared from cobalt acetate and cobalt acetyl acetonate were due probably to the unstable small Co particles forming Co silicates during reduction in H_2 and reaction.

Table 2

Results for CO hydrogenation[a]

Catalyst	Rate (gCH_2/ gcat./h)		CO Conversion (%)		Selectivity (%)		
	Initial	Steady-state	Initial	Steady-state	CH_4	C_2	C_3
Co/S-Ac	0.012	0.010	2.1	1.4	95	4.5	0.5
Co/S-AA	0.013	0.012	1.7	1.6	96	3.5	0.5
Co/S-Cl	0.007	0.006	0.9	0.8	84	13.0	3.0
Co/S-NO	0.176	0.167	23.4	22.7	95	5.0	-
Co/M-Ac	0.025	0.018	3.2	2.4	91	7.0	2.0
Co/M-AA	0.013	0.013	1.8	1.7	96	3.4	0.6
Co/M-Cl	0.024	0.018	3.3	2.4	97	2.5	0.5
Co/M-NO	0.449	0.323	59.8	47.6	82	6.0	2.0

[a] Reaction conditions are 220°C, 1 atm, and $H_2/CO = 10$

Acknowledgements. The financial supports from the Thailand Japan Technology Transfer Prject (TJTTP-JBIC) and the Thailand Research Fund (TRF) are gratefully acknowledged.

REFERENCES

1. R.B. Anderson: *The Fischer-Tropsch Synthesis*, Academic Press, San Diego 1984.
2. J.G. Goodwin, Jr.: *Prep. ACS. Div. Petr. Chem.*, **36**, 156 (1991).
3. D. Yin, W. Li, W. Yang, H. Xiang, Y. Sun, B. Zhong, S. Peng: *Micropor. Mesopor. Mater.*, **47**, 15 (2001).
4. J. Panpranot, J.G. Goodwin, Jr., A. Sayari: *Catal. Today*, **77**, 269 (2002).
5. Y. Wang, M. Noguchi, Y. Takahashi, Y. Ohtsuka: *Catal. Today*, **68**, 3 (2001).
6. A.Y. Khodakov, A. Griboval-Constant, R. Bechara, V.L. Zholobenko: *J. Catal.*, **206**, 230 (2002).
7. A. Martinez, C. Lopez, F. Marquez, I. Diaz: *J. Catal.*, **220**, 486 (2003).
8. J. Panpranot, J.G. Goodwin, Jr., A. Sayari: *J. Catal.*, **211**, 530 (2002).
9. M. Kruk, M. Jaronice, A. Sayari: *Micropor. Mesopor. Mater.*, **35-36**, 545 (2000).
10. J. Panpranot, S. Kaewgun, P. Praserthdam, J.G. Goodwin, Jr.: *Catal. Lett.*, **91**, 95 (2003).
11. A.M. Hilmen, D. Schanke, A. Holmen: *Catal. Lett.*, **38**, 143 (1996).
12. Y. Zhang, D. Wei, S. Hammache, J.G. Goodwin, Jr.: *J. Catal.*, **188**, 281 (1999).
13. R.C. Reuel, C.H. Bartholomew: *J. Catal.*, **85**, 63 (1984).
14. B. Ernst, S. Libs, P. Chaumette, A. Kiennemann, *Appl. Catal. A*, **186**, 145 (1999).
15. A. Kogelbauer, J.C. Weber, J.G. Goodwin, Jr.: *Catal. Lett.*, **34**, 259 (1995).
16. J.M. Jablonski, M. Wolcyrz, L. Krajczyk: *J. Catal.*, **173**, 530 (1998).

Catalysis Letters Vol. 103, Nos. 1–2, September 2005 (© 2005)
DOI: 10.1007/s10562-005-6504-8

Characteristics and catalytic properties of alumina–zirconia mixed oxides prepared by a modified Pechini method

Patta Soisuwan[a,b], Dean C. Chambers[c], David L. Trimm[b,c], Okorn Mekasuwandumrong[d], Joongjai Panpranot[a], and Piyasan Praserthdam[a,*]

[a]*Centre of Excellence on Catalysis and Catalytic Reaction Engineering, Department of Chemical Engineering, Faculty of Engineering, Chulalongkorn University, Bangkok, 10330 Thailand*
[b]*School of Chemical Engineering and Industrial Chemistry, University of New South Wales, Sydney, NSW, 2052 Australia*
[c]*CSIRO Petroleum, Private Bag 10, Clayton South, VIC, 3169 Australia*
[d]*Department of Chemical Engineering, Faculty of Engineering and Industrial Technology, Silpakorn University, Nakon Pathom, 73000 Thailand*

Received 22 November 2004; accepted 5 May 2005

A modified Pechini method was used to prepare alumina–zirconia mixed oxides at three different molar ratios. For comparison, pure alumina and pure zirconia were prepared using the same method. The mixed oxides were characterised by the BET method for surface area, X-ray diffraction, CO_2 and NH_3 temperature-programmed desorption. Elimination of 2-propanol was used as a probe reaction to characterise the surface of the mixed oxides. The modified Pechini preparation resulted in a poor acid–base strength of alumina surface resulting in high acetone selectivity where imperfect crystal structure of the tetragonal zirconia favoured high propylene production in 2-propanol elimination at 200 °C.

KEY WORDS: alumina; zirconia; mixed oxide; Pechini method; 2-propanol.

1. Introduction

The sol–gel technique is widely used for preparation of ceramic materials, especially mixed oxides, because lower temperatures are required compared to conventional ceramic mixing processes and it improves dispersion and homogeneity [1]. Different precursors have been used to prepare sol–gel materials, particularly metal alkoxides [2–10] and citric acid (CA) complexes [11–13]. The materials obtained from both processes are quite similar but gel formation is approached under different conditions. Zirconia prepared by the sol–gel method, however, usually possesses low surface area. Recently, it has been reported that solid powders were successfully prepared by the modified Pechini method [14,15], in which CA and ethylene glycol are polymerised around metal ions. In 1963, Pechini *et al.* discovered a preparation method of mixed oxides, which can be applied for ceramic and dielectric materials. Because of homogeneous starting solution producing resin intermediate and then resulting in oxide by ignition, this technique leads to closer combination of mixed oxides, which may enhance strong interaction between metal ions. Moreover, high surface area of solid powders is usually obtained by this method, which could bring about high dispersion of metal loading and consequently high active sites for catalytic reactions [15]. In this study, a modified Pechini method was used to prepare alumina, zirconia and alumina–zirconia mixed oxides. Zirconia toughened alumina is generally employed in ceramic application because of its well-known mechanical property, moreover, recently mixed oxide of zirconia and alumina has been introduced in medical application as a biocompatible nano-composite [16]. In catalytic reaction, zirconia alumina has been used as catalyst and/or support because of its surface property, stability and mechanical property. Modification of the mixed oxide by sulfate is well known and showed very good activity of isomerisation [17]. Zirconia alumina at different ratios was prepared to improve surface properties by well-dispersed sol gel preparation. The effect of Al/Zr ratio on the characteristics and catalytic properties of the alumina–zirconia mixed oxides was investigated by means of nitrogen physisorption (BET), X-ray diffraction (XRD) and CO_2 and NH_3 temperature-programmed desorption (TPD). Elimination reactions of 2-propanol were used to determine the catalytic activity of the oxides.

* To whom correspondence should be addressed.
E-mail: piyasan.p@chula.ac.th

2. Experimental

2.1. Preparation of alumina–zirconia mixed oxides

Alumina–zirconia mixed oxides were prepared using a modified Pechini method in the same manner as that of [14,15] with Al/Zr molar ratios of 1:3, 2:3, 1:1, and 3:1. For comparison, pure alumina and zirconia were prepared by the same method. Aluminium nitrate [$Al(NO_3)_3 \cdot 9H_2O$] and zirconyl nitrate [$ZrO(NO_3)_2 \cdot xH_2O$] were used as precursors. The nitrate salts

were dissolved in separately water. Aqueous CA solution was prepared and its pH was adjusted to ca. 1 by addition of 35% nitric acid. CA solution was added to the zirconyl nitrate solution at a molar ratio of [Al+Zr:CA]=3:7. Aluminium nitrate solution was added to the zirconyl citrate complex and finally ethylene glycol was added. The pH of the solution was adjusted to 7, by addition of 35% ammonium hydroxide, to form an alumina gel [18]. The resulting solution was heated under vacuum in a rotary evaporator at 90–100 °C until it became viscous and yellow. After the vacuum was removed, the solution became black and gel-like. This material was removed from the system, dried at 100 °C overnight and calcined in flowing air, with a heating rate of 1 °C/min and final temperature of 500 °C held for 6 h. In the case of pure zirconia, the gel-like material did not appear during the rotary evaporation step, even after many hours, but appeared after the vacuum was removed.

2.2. Characterisation

Characterisation of the samples using various analysis techniques was carried out on the calcined samples. The surface area was measured by nitrogen physisorption at 77 K after outgassing at 300 °C. Surface areas were determined by the BET method and pore-size distribution by the BJH method. The crystal structures were characterised by XRD (Siemens D5000) using nickel filtered CuK_α radiation. TPD of CO_2 was used to characterise the basic sites of the oxides. Samples were pre-treated at 400 °C for 1 h in He, then saturated with CO_2 (99.99%) at 35 °C for 3 h. Desorption of CO_2, by heating at 10 °C/min to 400 °C, was measured using a GOW-MAC thermal conductivity detector (TCD). TPD of NH_3 (Micromeritics Autochem 2910) was used to characterise the acid sites. Samples were pre-treated in He at 400 °C for 1 h and saturated with 10%NH_3/He at 100 °C for 2 h. Adsorbed NH_3 was removed by flowing He (10 mL/min) while heating at 10 °C/min to 400 °C and detected by TCD.

2.3. Catalytic activity

Catalyst testing was carried out at atmospheric pressure in a quartz fixed-bed reactor. The catalyst sample was treated in air at 400 °C for 1 h prior to the reaction to remove adsorbed H_2O and CO_2. Elimination of 2-propanol was carried out at 150, 200 and 250 °C as in [19,20]. Helium (~12 mL/min) was bubbled through 2-propanol at fixed temperature (~50 °C) to give a concentration of 12-mol% 2-propanol in He flowing through 100 mg of catalyst. Typical space velocities (WHSV) were in the range of 20–200 h^{-1} as in [20]. Reaction products were analysed using a Shimadzu GC-14A gas chromatograph with a flame ionisation detector and a column containing 15%-Carbowax 1000 supported on Chromosorb W. Measurements were taken every 20 min until a steady state was reached, typically after about 2 h. The reaction products were propylene, acetone and diisopropyl ether.

3. Results

3.1. N_2 adsorption

The BET surface areas and BJH pore size distributions of the mixed oxides solid powders after calcination for 6 h at 500 °C are given in table 1. The surface areas increased with alumina content. For pure zirconia, most of the pores were macro-sized (>50 nm), while the mixed oxides had pore volumes more evenly distributed between micro-, meso- and macropores. Pure alumina had most of its pore volume in the meso and macro range.

3.2. XRD analysis

Crystal phases of the mixed oxides were identified by XRD. Figure 1 shows the XRD patterns of pure zirconia, $Al_{40}Zr_{60}$ and pure alumina after calcination at 1000 °C. The identified crystal structures and crystallite sizes after ignition at 500 °C and calcinations at 800 and 1000 °C calculated using Scherrer's equation are shown in table 2.Calcination of zirconia at 500 °C and above gave mostly tetragonal phase, with the monoclinic phase becoming dominant at 1000 °C. Alumina was amorphous after calcination at 500 °C and changed from θ to α between 800 and 1000 °C. In the mixed oxide sample, no alumina XRD peaks could be detected at any temperature. The sample calcined at 500 °C was completely amorphous while only tetragonal zirconia peaks were detected even at 1000 °C. In all cases, the crystallite sizes increased with increasing calcinations temperature.

Table 1
Surface area and pore size distribution of zirconia, alumina and mixed oxides

Composition (mol%)	BET surface area (g/m^2)	BJH pore size distribution (%)		
		Micro <2 nm	Meso 2–50 nm	Macro >50 nm
Zirconia	56	6.2	24.1	69.7
$Al_{25}Zr_{75}$	70	26.4	43.8	29.7
$Al_{40}Zr_{60}$	182	24.5	33.9	41.7
$Al_{75}Zr_{25}$	228	34.2	30.5	35.4
Alumina	319	13.6	44.7	41.7

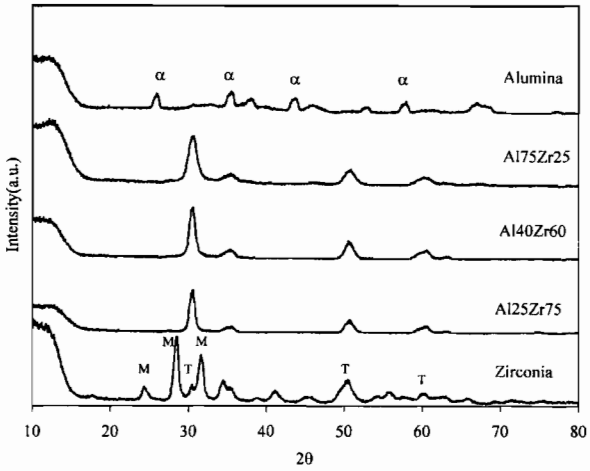

Figure 1. XRD diffraction pattern of zirconia, alumina and zirconia alumina mixed oxide calcined at 1000 °C.

Table 2
Crystal structure and size of zirconia crystals in zirconia, alumina and mixed oxides

Sample	Crystal structure (crystal size, nm)		
	Calcination temperature		
	500 °C	800 °C	1000 °C
Zirconia	T(13)	T(26)	M(31),T
$Al_{25}Zr_{75}$	A	T(13)	T(28)
$Al_{40}Zr_{60}$	A	T(14)	T(19)
$Al_{75}Zr_{25}$	A	A	T(13)
Alumina	A	θ	α

Symbols A, M and T indicate amorphous, monoclinic and tetragonal phases of zirconia (or pure alumina) respectively.
Symbols θ and α indicate theta and alpha phases of alumina respectively.

3.3. CO_2 temperature programmed desorption

Basicity of the catalysts was measured by CO_2 temperature programmed desorption up to 400 °C. Figure 2 shows the CO_2 TPD profiles of all the catalyst samples. In all cases, a single desorption peak was observed around 100–115 °C. The CO_2 desorption temperature of pure zirconia and pure alumina were found to be slightly lower than that of the mixed oxides. The amounts of CO_2 desorbed from the mixed oxides, pure alumina and pure zirconia were calculated by integrating the areas of CO_2 TPD profiles and are reported in table 3.

3.4. NH_3 temperature programmed desorption

Acidity of the catalysts was measured by NH_3-TPD. The NH_3 TPD profiles for all the catalysts are shown in figure 3. None of the materials tested showed distinct NH_3 desorption peaks up to 400 °C. The broad desorption peaks below 200 °C occurred at slightly higher temperature for two of the mixed oxides than for pure alumina or zirconia. This suggests that the acid strength of those mixed oxides is slightly greater than the pure oxides. Table 3 also shows the amounts of NH_3 desorbed from each sample.

3.5. Reaction test

The catalytic activities of the mixed oxide were tested in the elimination reactions of 2-propanol at 150, 200, and 250 °C. The results are given in table 4. At 150 °C,

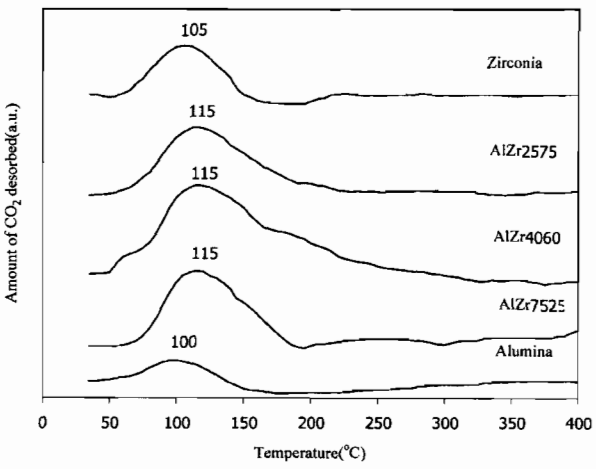

Figure 2. Temperature programmed desorption of CO_2 on mixed oxide, pure zirconia and pure alumina.

the elimination product was almost entirely acetone for all catalysts. At 200 °C, the product distribution depended on the catalyst composition. Catalysts high in alumina content produced mainly acetone, while those high in zirconia produced large amounts of propylene. Traces of diisopropyl ether appeared at this temperature. At higher temperature (250 °C) the product distribution changed again, to favour propylene production over all materials. Catalysts high in alumina also produced significant amounts of diisopropyl ether at this temperature. It should be noted that alumina activated in oxygen can exhibit dehydrogenation activity that may exceed considerably the dehydration selectivity [21]. However, the effect of oxygen pretreatment was not observed in this study (no oxidation reaction) since one would expect changes in selectivity of acetone with increasing reaction time due to consumption of oxygen covering the catalyst surface.

Table 3
Quantities of $CO_2$and NH_3 desorbed from zirconia, alumina and mixed oxides

Sample	CO_2 desorbed (μmol/g)	NH_3 desorbed (μmol/g)
Zirconia	172	202
$Al_{25}Zr_{75}$	279	478
$Al_{40}Zr_{60}$	632	752
$Al_{75}Zr_{25}$	485	830
Alumina	146	69

4. Discussion

The macropore system may occur after removal of organic material polymerised from CA and ethylene glycol in fresh gel. It is suggested that under these preparation conditions, well dispersed alumina and zirconia influencing orientation of alumina and zirconia crystal structure of the mixed oxide. Using this method, tetragonal phase of pure zirconia were obtained after calcination at 500 °C. The tetragonal phase zirconia is thermodynamically stable at a temperature above 1170 °C [22]. However, removal of combustible organic materials at 500 °C during preparation could result in sufficient energy to arrange the zirconia structure in tetragonal form.

Surface properties of pure zirconia, pure alumina and the mixed oxides might be classified into two types by probe molecule adsorption; CO_2 and NH_3 probe molecules. The interaction between CO_2 probe molecule and zirconia or mixed oxides surfaces might be physical adsorption in accordance with a result of Li *et al.* [23] showing desorption of CO_2 physical bonding on zirconia surface is around 100 °C. Desorption temperatures might be improved to be higher after atomically mixing zirconia with alumina. This is probably due to the interaction between aluminium, oxygen and zirconium ions in the mixed oxide increasing the physical strength between surface oxygen and CO_2 probe molecule.

It is known that the reaction pathways of 2-propanol elimination forming dehydration and dehydrogenation products occur on different nature and strength of acid–base sites [20]. Different mechanisms have been derived

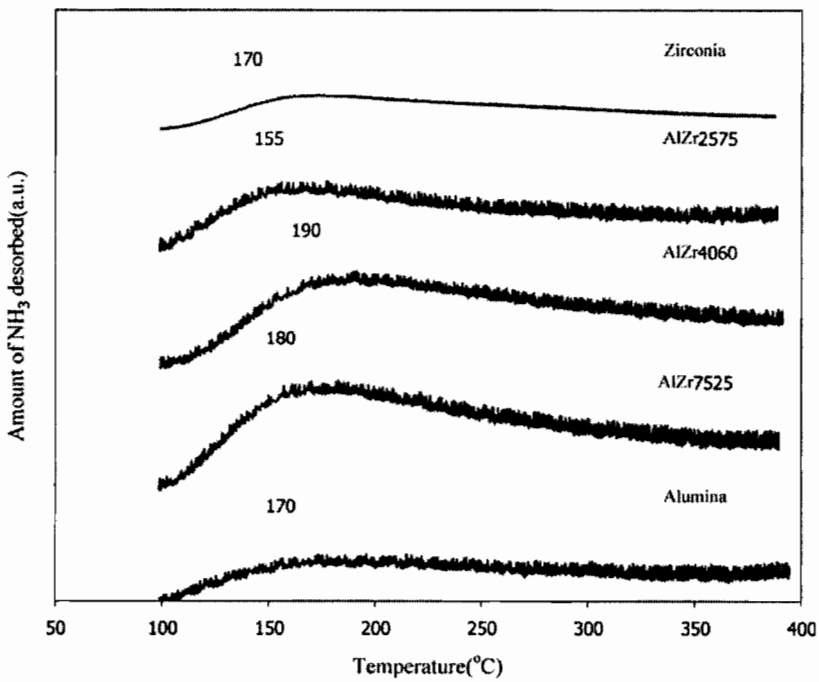

Figure 3. Temperature programmed desorption of NH_3 on mixed oxide, pure zirconia and pure alumina.

Table 4
Catalyst activity and selectivity during elimination of 2-propanol

Sample	T = 150 °C				T = 200 °C				T = 250 °C			
	% Conversion	S_P	S_A (%)	S_{DIP}	% Conversion	S_P	S_A (%)	S_{DIP}	% Conversion	S_P	S_A(%)	S_{DIP}
Alumina	3.5	2.0	98.0	0.0	9.8	1.6	98.1	0.3	36.6	66.3	24.1	9.5
$Al_{75}Zr_{25}$	5.5	1.3	98.7	0.0	2.5	6.3	92.6	1.1	6.9	66.6	28.7	4.6
$Al_{40}Zr_{60}$	0.3	10.2	89.8	0.0	1.0	7.7	92.3	0.0	10.7	48.3	48.8	2.9
$Al_{25}Zr_{75}$	2.2	2.0	98.0	0.0	1.3	27.5	71.7	0.8	7.5	64.3	34.5	1.2
Zirconia	1.0	8.9	91.1	0.0	4.4	89.2	10.2	0.6	7.5	75.2	24.5	0.3

based on individual transition states including E_1, E_2, and E_{1cB} [20,25]. E_1 mechanism requires strong acidic catalysts to form carbenium ions by abstraction of OH-group. The carbenium ions are rearranged via isomerisation and abstracted hydrogen resulting in different kind of alkenes [25].

In this study, the NH_3 temperature programmed desorption results exhibited a single peak below 200 °C suggesting that the acidic strength was probably unable to abstract OH groups. The E_1 mechanism then can be excluded. For E_2 mechanism, reaction occurs on dual acid–base sites to simultaneously eliminate a proton and hydroxyl group producing the main product alkene whereas for E_{1cB} mechanism, strong basic sites are required in order to firstly detach β hydrogen and then eliminate hydroxyl group [25].

Recently, Díez *et al.* [20,26] propose a mechanism slightly different from E_{1cB} mechanism in which reaction takes place via acid–base sites of imbalanced strength. Adsorption of OH group occurs on weak acid–base sites to form a surface propoxide intermediate. The most acidic hydrogen of alcohol is attacked by strong base site (the surface oxygen), in contrast, the Lewis acid site (the surface cation) attacks the oxygen of alcohol resulting in rupture of hydroxyl groups. Two pathways were proposed after forming propoxide on the surface: (a) dehydration of 2-propanol where acetone is a result of abstraction α-hydrogen and (b) dehydrogenation of 2-propanol producing propylene by detaching β-hydrogen. The products of the E_{1cB} mechanism could be either propylene or acetone or both depending on the strength of base site. However, the base site detaching β-hydrogen is stronger than the one detaching α-hydrogen. Waugh *et al.* [26,27] found that the activation energy of α-hydrogen abstraction is lower than the activation energy of β-hydrogen abstraction.

Generally, elimination of 2-propanol on alumina produces propylene as the main product via E_2 mechanism due to amphoteric properties of alumina [19, 28]. Dominuguez *et al.* [19] showed that γ-alumina gave propylene selectivity more than 80% in a range of reaction temperature 180–240 °C. However, in this study we observed that most of the propanol elimination products over the Pechini alumina were more than 90% acetone. Disordered structure of the Pechini amorphous alumina could result in an imbalanced strength of acid–base sites and the reaction pathway might occur via E_{1cB} proposed by Díez *et al.* The weak physically adsorbing CO_2 site of alumina as shown by the low temperature CO_2 desorption peak in figure 2 could bring about abstraction of α-hydrogen mostly resulting in acetone formation. This might be representative of very poor basicity of alumina surface.

Similar to the pure alumina, the Pechini alumina–zirconia mixed oxides converted to propanol towards acetone with more than 70% selectivity at 150 and 200 °C. Increasing zirconia content in the mixed oxides resulted in a slight decrease in acetone and increase in propylene selectivity at 200 °C. The propylene formation may be ascribed to zirconia. The E_{1cB} mechanism appeared to dominate over the alumina–zirconia mixed oxides. Although the CO_2 desorption peaks of the mixed oxides shifted towards 115 °C, the strength of basicity would not be very effective to abstract β-hydrogen. Increasing propylene selectivity over the alumina–zirconia mixed oxides was probably affected by dual acid–base property of zirconia via the E_2 mechanism. This is in a good agreement with the work reported by Tanabe [29], in which 2-propanol elimination on zirconia catalysts proceed by acid–base site bifunctional catalysis. The orientation of these sites plays an importance role in governing the reaction [30]. However, the orientation of alumina–zirconia mixed oxides structure would be undisciplined resulting in a decrease in acid–base bifunctional property. Therefore, the E_2 mechanism would not dominate over the alumina–zirconia mixed oxides.

Conversion of propanol towards propylene over tetragonal zirconia was observed with more than 80% selectivity at 200 °C. The well-ordered structure of tetragonal zirconia exhibited high selectivity of propylene via the dominant E_2 mechanism. In contrast, partly imperfect crystal of tetragonal zirconia could result in imbalanced acid–base site leading to acetone formation via the E_{1cB} mechanism.

5. Conclusions

The alumina–zirconia mixed oxides produced by the modified Pechini method resulted in combination of aluminium and zirconium atoms. Due to good

dispersion of aluminium and zirconium ions, the mixed oxides present only amorphous form. Apparently, the interaction between Al, Zr, and O in the mixed oxides resulted in higher physical strength of CO_2 adsorption. The modified acidity was, however, ambiguous because all the catalyst samples exhibited low acidity. The imbalance strength of acid–base site due to the imperfect crystal structure of all the catalysts resulted in higher acetone formation via E_{1cB} mechanism. However, 90% propylene selectivity was obtained on pure zirconia prepared by the modified Pechini method and 200 °C reaction temperature.

Acknowledgments

The authors would like to thank the Cooperative Research Network, Thai Ministry of Education, the Thailand Research Fund, the University of New South Wales and CSIRO for financial support. The authors also thank Mr Praharso, Ms Sarah Watson, Mr Richard Burgess and Mr John Starling and Dr Manh Hoang for their support.

References

[1] G. Ertl, H. Knözinger and J. Weitkamp, *Handbook of Heterogeneous Catalysis* (Wiley-VCH, City, 1997).
[2] J.C. Debsikdar, J. Non-Cryst. Solids 86 (1986) 231.
[3] R. Guinebretière, A. Dauger, A. Lecomte and H. Vesteghem, J. Non-Cryst. Solids 147&148 (1992) 542.
[4] J. Livage, F. Beteille, C. Roux, M. Chatry and P. Davidson, Acta mater. 46 (1998) 743.
[5] C. Stöcker and J. Baiker A., Non-Cryst. Solids 223 (1998) 165.
[6] M.M. Pineda, S. Castillo, T. López, R. Gómez, Cordero-Borboa and O. Novaro, Appl. Catal. B: Environ. 21 (1999) 79.
[7] J.L. Lakshmi, T.R.B. Jones, M. Gurgi and J.M. Miller, J. Mol. Catal. A: Chem. 152 (2000) 99.
[8] D.D. Jayaseelan, D.A. Rani, T. Nishikawa, H. Awaji and F.D. Gnanam, J. Euro. Ceram. Soc. 20 (2000) 267.
[9] A.C. Geiculescu and H.J. Rack, J. Non-Crytal. Solids 289 (2001) 53.
[10] Y. Hao, J. Li, X. Yang, X. Wang and L. Lu, Mat. Sci. Eng. A 367 (2004) 243.
[11] M. Ishii, M. Kakihana, K. Ishii, Y. Ikuma and M. Yoshimura, J. Mat. Res. Soc. 11(6) (1996) 1410.
[12] M. Kakihana, S. Kato, M. Yashima and M. Yoshimura, J. Alloys Comp. 280 (1998) 125.
[13] E.N.S. Muccillo, E.C.C. Souza and R. Muccillo, J. Alloys Comp. 344 (2002) 175.
[14] M.P. Pechini, Patent, 11 July (1967) 3,330,697.
[15] C.L. Robert, F. Ansart, C. Deloget, M. Gaudon and A. Rousset, Ceram. Int. 29 (2003) 151.
[16] Y.M. Kong, C.J. Bae, S.H. Lee, H.W. Kim and H.E. Kim, Biomaterials 26 (2005) 509.
[17] I.I. Abu, D.D. Das, H.K. Mishra and A.K. Dalai, J. Colloid Interface Sci. 267 (2003) 382.
[18] R. Mezei and K. Sinkó, Colloid Polym. Sci. 274 (1996) 1054.
[19] J.M. Dominguez, J.L. Hernandez and G. Sandoval, Appl. Cata. A: Gen. 197 (2000) 119.
[20] V.K. Díez, C.R. Apesteguía and J.I. Di Cosimo, J. Catal. 215 (2003) 220.
[21] B.H. Davis, J. Catal. 26 (1972) 348.
[23] P.D.L. Mercera, J.G. van Ommen, E.B.M. Doesburg, A.J. Burggraaf and J.R.H. Ross, Appl. Catal. 71 (1991) 363.
[23] Y. Li, D. He, Z. Cheng, C. Zu, J. Le and Q. Zhu, J. Mol. Catal. A: Chem. 175 (2001) 267.
[24] A. Davydov, *Molecular Spectroscopy of Oxide Catalyst Surfaces* (John Wiley & Sons, England, 2003).
[25] K. Tanabe, M. Misono, Y. Ono and H. Hattari, *New Solid Acids and Bases Their Catalyst Properties* (Kodansha, Tokyo, 1989).
[26] V.K. Díez, C.R. Apesteguía and J.I. Di Cosimo, Catal. Today 63 (2000) 53.
[27] K.C. Waugh, M. Bowker, R.W. Petts, H.D. Vanderwell and J. O'Malley, Appl. Catal. 25 (1986) 121.
[28] A. Gervasini, J. Fenyvesi and A. Auroux, Catal. Lett. 43 (1997) 219.
[29] K. Tanabe, Mat. Chem. Phys. 13 (1985) 347.
[30] S. Chokkaram and B.H. Davis, J. Mol. Catal. A: Chem. 118 (1997) 89.

Catalysis Letters Vol. 103, Nos. 1–2, September 2005 (© 2005)
DOI: 10.1007/s10562-005-6504-8

Characteristics and catalytic properties of alumina–zirconia mixed oxides prepared by a modified Pechini method

Patta Soisuwan[a,b], Dean C. Chambers[c], David L. Trimm[b,c], Okorn Mekasuwandumrong[d], Joongjai Panpranot[a], and Piyasan Praserthdam[a,*]

[a]*Centre of Excellence on Catalysis and Catalytic Reaction Engineering, Department of Chemical Engineering, Faculty of Engineering, Chulalongkorn University, Bangkok, 10330 Thailand*
[b]*School of Chemical Engineering and Industrial Chemistry, University of New South Wales, Sydney, NSW, 2052 Australia*
[c]*CSIRO Petroleum, Private Bag 10, Clayton South, VIC, 3169 Australia*
[d]*Department of Chemical Engineering, Faculty of Engineering and Industrial Technology, Silpakorn University, Nakon Pathom, 73000 Thailand*

Received 22 November 2004; accepted 5 May 2005

A modified Pechini method was used to prepare alumina–zirconia mixed oxides at three different molar ratios. For comparison, pure alumina and pure zirconia were prepared using the same method. The mixed oxides were characterised by the BET method for surface area, X-ray diffraction, CO_2 and NH_3 temperature-programmed desorption. Elimination of 2-propanol was used as a probe reaction to characterise the surface of the mixed oxides. The modified Pechini preparation resulted in a poor acid–base strength of alumina surface resulting in high acetone selectivity where imperfect crystal structure of the tetragonal zirconia favoured high propylene production in 2-propanol elimination at 200 °C.

KEY WORDS: alumina; zirconia; mixed oxide; Pechini method; 2-propanol.

1. Introduction

The sol–gel technique is widely used for preparation of ceramic materials, especially mixed oxides, because lower temperatures are required compared to conventional ceramic mixing processes and it improves dispersion and homogeneity [1]. Different precursors have been used to prepare sol–gel materials, particularly metal alkoxides [2–10] and citric acid (CA) complexes [11–13]. The materials obtained from both processes are quite similar but gel formation is approached under different conditions. Zirconia prepared by the sol–gel method, however, usually possesses low surface area. Recently, it has been reported that solid powders were successfully prepared by the modified Pechini method [14,15], in which CA and ethylene glycol are polymerised around metal ions. In 1963, Pechini *et al.* discovered a preparation method of mixed oxides, which can be applied for ceramic and dielectric materials. Because of homogeneous starting solution producing resin intermediate and then resulting in oxide by ignition, this technique leads to closer combination of mixed oxides, which may enhance strong interaction between metal ions. Moreover, high surface area of solid powders is usually obtained by this method, which could bring about high dispersion of metal loading and consequently high active sites for catalytic reactions [15]. In this study, a modified Pechini method was used to prepare alumina, zirconia and alumina–zirconia mixed oxides. Zirconia toughened alumina is generally employed in ceramic application because of its well-known mechanical property, moreover, recently mixed oxide of zirconia and alumina has been introduced in medical application as a biocompatible nano-composite [16]. In catalytic reaction, zirconia alumina has been used as catalyst and/or support because of its surface property, stability and mechanical property. Modification of the mixed oxide by sulfate is well known and showed very good activity of isomerisation [17]. Zirconia alumina at different ratios was prepared to improve surface properties by well-dispersed sol gel preparation. The effect of Al/Zr ratio on the characteristics and catalytic properties of the alumina–zirconia mixed oxides was investigated by means of nitrogen physisorption (BET), X-ray diffraction (XRD) and CO_2 and NH_3 temperature-programmed desorption (TPD). Elimination reactions of 2-propanol were used to determine the catalytic activity of the oxides.

* To whom correspondence should be addressed.
E-mail: piyasan.p@chula.ac.th

2. Experimental

2.1. Preparation of alumina–zirconia mixed oxides

Alumina–zirconia mixed oxides were prepared using a modified Pechini method in the same manner as that of [14,15] with Al/Zr molar ratios of 1:3, 2:3, 1:1, and 3:1. For comparison, pure alumina and zirconia were prepared by the same method. Aluminium nitrate [$Al(NO_3)_3 \cdot 9H_2O$] and zirconyl nitrate [$ZrO(NO_3)_2 \cdot xH_2O$] were used as precursors. The nitrate salts

were dissolved in separately water. Aqueous CA solution was prepared and its pH was adjusted to ca. 1 by addition of 35% nitric acid. CA solution was added to the zirconyl nitrate solution at a molar ratio of [Al+Zr:CA]=3:7. Aluminium nitrate solution was added to the zirconyl citrate complex and finally ethylene glycol was added. The pH of the solution was adjusted to 7, by addition of 35% ammonium hydroxide, to form an alumina gel [18]. The resulting solution was heated under vacuum in a rotary evaporator at 90–100 °C until it became viscous and yellow. After the vacuum was removed, the solution became black and gel-like. This material was removed from the system, dried at 100 °C overnight and calcined in flowing air, with a heating rate of 1 °C/min and final temperature of 500 °C held for 6 h. In the case of pure zirconia, the gel-like material did not appear during the rotary evaporation step, even after many hours, but appeared after the vacuum was removed.

2.2. Characterisation

Characterisation of the samples using various analysis techniques was carried out on the calcined samples. The surface area was measured by nitrogen physisorption at 77 K after outgassing at 300 °C. Surface areas were determined by the BET method and pore-size distribution by the BJH method. The crystal structures were characterised by XRD (Siemens D5000) using nickel filtered CuK_α radiation. TPD of CO_2 was used to characterise the basic sites of the oxides. Samples were pre-treated at 400 °C for 1 h in He, then saturated with CO_2 (99.99%) at 35 °C for 3 h. Desorption of CO_2, by heating at 10 °C/min to 400 °C, was measured using a GOW-MAC thermal conductivity detector (TCD). TPD of NH_3 (Micromeritics Autochem 2910) was used to characterise the acid sites. Samples were pre-treated in He at 400 °C for 1 h and saturated with 10%NH_3/He at 100 °C for 2 h. Adsorbed NH_3 was removed by flowing He (10 mL/min) while heating at 10 °C/min to 400 °C and detected by TCD.

2.3. Catalytic activity

Catalyst testing was carried out at atmospheric pressure in a quartz fixed-bed reactor. The catalyst sample was treated in air at 400 °C for 1 h prior to the reaction to remove adsorbed H_2O and CO_2. Elimination of 2-propanol was carried out at 150, 200 and 250 °C as in [19,20]. Helium (~12 mL/min) was bubbled through 2-propanol at fixed temperature (~50 °C) to give a concentration of 12-mol% 2-propanol in He flowing through 100 mg of catalyst. Typical space velocities (WHSV) were in the range of 20–200 h^{-1} as in [20]. Reaction products were analysed using a Shimadzu GC-14A gas chromatograph with a flame ionisation detector and a column containing 15%-Carbowax 1000 supported on Chromosorb W. Measurements were taken every 20 min until a steady state was reached, typically after about 2 h. The reaction products were propylene, acetone and diisopropyl ether.

3. Results

3.1. N_2 adsorption

The BET surface areas and BJH pore size distributions of the mixed oxides solid powders after calcination for 6 h at 500 °C are given in table 1. The surface areas increased with alumina content. For pure zirconia, most of the pores were macro-sized (>50 nm), while the mixed oxides had pore volumes more evenly distributed between micro-, meso- and macropores. Pure alumina had most of its pore volume in the meso and macro range.

3.2. XRD analysis

Crystal phases of the mixed oxides were identified by XRD. Figure 1 shows the XRD patterns of pure zirconia, $Al_{40}Zr_{60}$ and pure alumina after calcination at 1000 °C. The identified crystal structures and crystallite sizes after ignition at 500 °C and calcinations at 800 and 1000 °C calculated using Scherrer's equation are shown in table 2.Calcination of zirconia at 500 °C and above gave mostly tetragonal phase, with the monoclinic phase becoming dominant at 1000 °C. Alumina was amorphous after calcination at 500 °C and changed from θ to α between 800 and 1000 °C. In the mixed oxide sample, no alumina XRD peaks could be detected at any temperature. The sample calcined at 500 °C was completely amorphous while only tetragonal zirconia peaks were detected even at 1000 °C. In all cases, the crystallite sizes increased with increasing calcinations temperature.

Table 1
Surface area and pore size distribution of zirconia, alumina and mixed oxides

Composition (mol%)	BET surface area (g/m^2)	BJH pore size distribution (%)		
		Micro <2 nm	Meso 2–50 nm	Macro >50 nm
Zirconia	56	6.2	24.1	69.7
$Al_{25}Zr_{75}$	70	26.4	43.8	29.7
$Al_{40}Zr_{60}$	182	24.5	33.9	41.7
$Al_{75}Zr_{25}$	228	34.2	30.5	35.4
Alumina	319	13.6	44.7	41.7

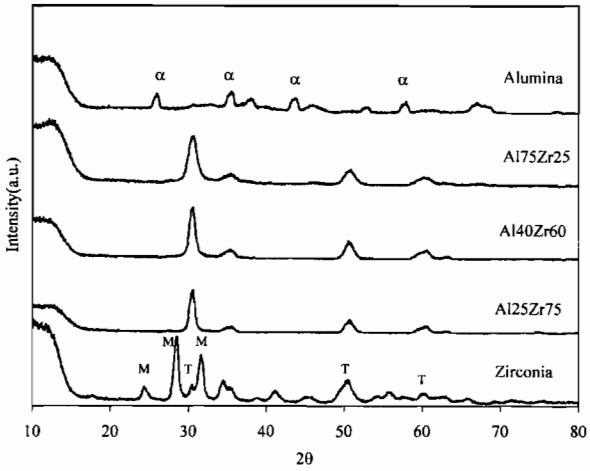

Figure 1. XRD diffraction pattern of zirconia, alumina and zirconia alumina mixed oxide calcined at 1000 °C.

Table 2
Crystal structure and size of zirconia crystals in zirconia, alumina and mixed oxides

Sample	Crystal structure (crystal size, nm)		
	Calcination temperature		
	500 °C	800 °C	1000 °C
Zirconia	T(13)	T(26)	M(31),T
$Al_{25}Zr_{75}$	A	T(13)	T(28)
$Al_{40}Zr_{60}$	A	T(14)	T(19)
$Al_{75}Zr_{25}$	A	A	T(13)
Alumina	A	θ	α

Symbols A, M and T indicate amorphous, monoclinic and tetragonal phases of zirconia (or pure alumina) respectively.
Symbols θ and α indicate theta and alpha phases of alumina respectively.

3.3. CO_2 temperature programmed desorption

Basicity of the catalysts was measured by CO_2 temperature programmed desorption up to 400 °C. Figure 2 shows the CO_2 TPD profiles of all the catalyst samples. In all cases, a single desorption peak was observed around 100–115 °C. The CO_2 desorption temperature of pure zirconia and pure alumina were found to be slightly lower than that of the mixed oxides. The amounts of CO_2 desorbed from the mixed oxides, pure alumina and pure zirconia were calculated by integrating the areas of CO_2 TPD profiles and are reported in table 3.

3.4. NH_3 temperature programmed desorption

Acidity of the catalysts was measured by NH_3-TPD. The NH_3 TPD profiles for all the catalysts are shown in figure 3. None of the materials tested showed distinct NH_3 desorption peaks up to 400 °C. The broad desorption peaks below 200 °C occurred at slightly higher temperature for two of the mixed oxides than for pure alumina or zirconia. This suggests that the acid strength of those mixed oxides is slightly greater than the pure oxides. Table 3 also shows the amounts of NH_3 desorbed from each sample.

3.5. Reaction test

The catalytic activities of the mixed oxide were tested in the elimination reactions of 2-propanol at 150, 200, and 250 °C. The results are given in table 4. At 150 °C,

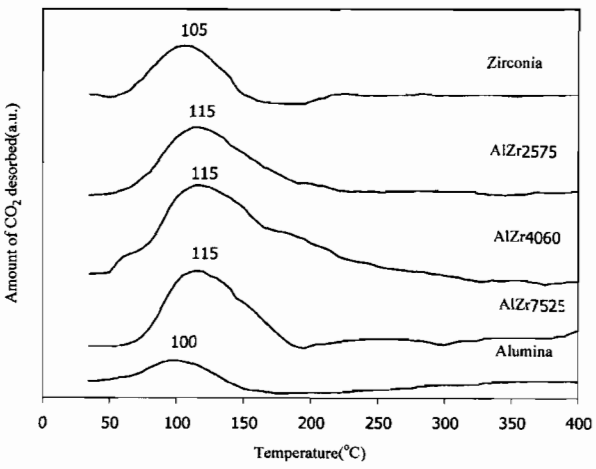

Figure 2. Temperature programmed desorption of CO_2 on mixed oxide, pure zirconia and pure alumina.

the elimination product was almost entirely acetone for all catalysts. At 200 °C, the product distribution depended on the catalyst composition. Catalysts high in alumina content produced mainly acetone, while those high in zirconia produced large amounts of propylene. Traces of diisopropyl ether appeared at this temperature. At higher temperature (250 °C) the product distribution changed again, to favour propylene production over all materials. Catalysts high in alumina also produced significant amounts of diisopropyl ether at this temperature. It should be noted that alumina activated in oxygen can exhibit dehydrogenation activity that may exceed considerably the dehydration selectivity [21]. However, the effect of oxygen pretreatment was not observed in this study (no oxidation reaction) since one would expect changes in selectivity of acetone with increasing reaction time due to consumption of oxygen covering the catalyst surface.

Table 3
Quantities of $CO_2$and NH_3 desorbed from zirconia, alumina and mixed oxides

Sample	CO_2 desorbed (μmol/g)	NH_3 desorbed (μmol/g)
Zirconia	172	202
$Al_{25}Zr_{75}$	279	478
$Al_{40}Zr_{60}$	632	752
$Al_{75}Zr_{25}$	485	830
Alumina	146	69

4. Discussion

The macropore system may occur after removal of organic material polymerised from CA and ethylene glycol in fresh gel. It is suggested that under these preparation conditions, well dispersed alumina and zirconia influencing orientation of alumina and zirconia crystal structure of the mixed oxide. Using this method, tetragonal phase of pure zirconia were obtained after calcination at 500 °C. The tetragonal phase zirconia is thermodynamically stable at a temperature above 1170 °C [22]. However, removal of combustible organic materials at 500 °C during preparation could result in sufficient energy to arrange the zirconia structure in tetragonal form.

Surface properties of pure zirconia, pure alumina and the mixed oxides might be classified into two types by probe molecule adsorption; CO_2 and NH_3 probe molecules. The interaction between CO_2 probe molecule and zirconia or mixed oxides surfaces might be physical adsorption in accordance with a result of Li *et al.* [23] showing desorption of CO_2 physical bonding on zirconia surface is around 100 °C. Desorption temperatures might be improved to be higher after atomically mixing zirconia with alumina. This is probably due to the interaction between aluminium, oxygen and zirconium ions in the mixed oxide increasing the physical strength between surface oxygen and CO_2 probe molecule.

It is known that the reaction pathways of 2-propanol elimination forming dehydration and dehydrogenation products occur on different nature and strength of acid–base sites [20]. Different mechanisms have been derived

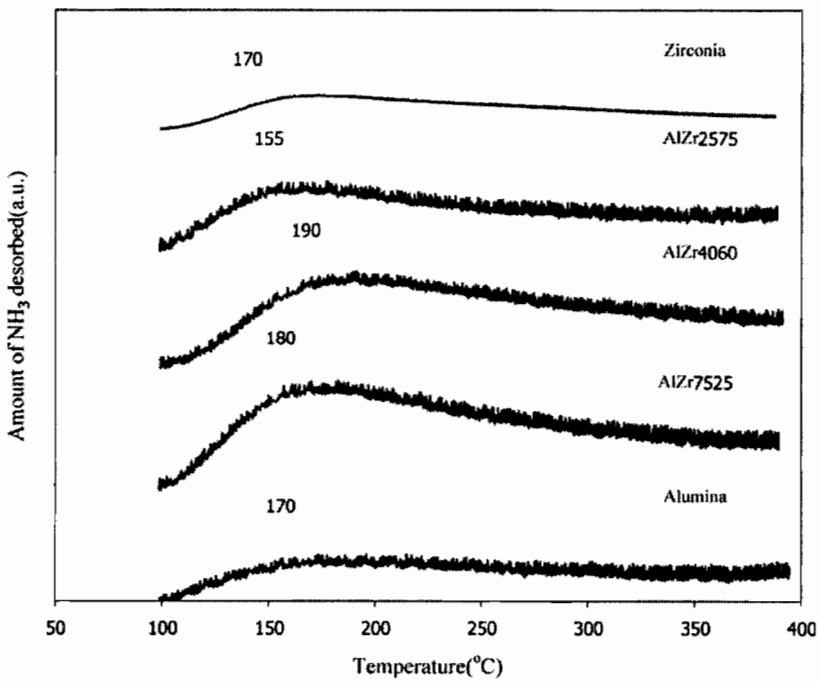

Figure 3. Temperature programmed desorption of NH_3 on mixed oxide, pure zirconia and pure alumina.

Table 4
Catalyst activity and selectivity during elimination of 2-propanol

Sample	T = 150 °C				T = 200 °C				T = 250 °C			
	% Conversion	S_P	S_A (%)	S_{DIP}	% Conversion	S_P	S_A (%)	S_{DIP}	% Conversion	S_P	S_A(%)	S_{DIP}
Alumina	3.5	2.0	98.0	0.0	9.8	1.6	98.1	0.3	36.6	66.3	24.1	9.5
$Al_{75}Zr_{25}$	5.5	1.3	98.7	0.0	2.5	6.3	92.6	1.1	6.9	66.6	28.7	4.6
$Al_{40}Zr_{60}$	0.3	10.2	89.8	0.0	1.0	7.7	92.3	0.0	10.7	48.3	48.8	2.9
$Al_{25}Zr_{75}$	2.2	2.0	98.0	0.0	1.3	27.5	71.7	0.8	7.5	64.3	34.5	1.2
Zirconia	1.0	8.9	91.1	0.0	4.4	89.2	10.2	0.6	7.5	75.2	24.5	0.3

based on individual transition states including E_1, E_2, and E_{1cB} [20,25]. E_1 mechanism requires strong acidic catalysts to form carbenium ions by abstraction of OH-group. The carbenium ions are rearranged via isomerisation and abstracted hydrogen resulting in different kind of alkenes [25].

In this study, the NH_3 temperature programmed desorption results exhibited a single peak below 200 °C suggesting that the acidic strength was probably unable to abstract OH groups. The E_1 mechanism then can be excluded. For E_2 mechanism, reaction occurs on dual acid–base sites to simultaneously eliminate a proton and hydroxyl group producing the main product alkene whereas for E_{1cB} mechanism, strong basic sites are required in order to firstly detach β hydrogen and then eliminate hydroxyl group [25].

Recently, Díez *et al.* [20,26] propose a mechanism slightly different from E_{1cB} mechanism in which reaction takes place via acid–base sites of imbalanced strength. Adsorption of OH group occurs on weak acid–base sites to form a surface propoxide intermediate. The most acidic hydrogen of alcohol is attacked by strong base site (the surface oxygen), in contrast, the Lewis acid site (the surface cation) attacks the oxygen of alcohol resulting in rupture of hydroxyl groups. Two pathways were proposed after forming propoxide on the surface: (a) dehydration of 2-propanol where acetone is a result of abstraction α-hydrogen and (b) dehydrogenation of 2-propanol producing propylene by detaching β-hydrogen. The products of the E_{1cB} mechanism could be either propylene or acetone or both depending on the strength of base site. However, the base site detaching β-hydrogen is stronger than the one detaching α-hydrogen. Waugh *et al.* [26,27] found that the activation energy of α-hydrogen abstraction is lower than the activation energy of β-hydrogen abstraction.

Generally, elimination of 2-propanol on alumina produces propylene as the main product via E_2 mechanism due to amphoteric properties of alumina [19, 28]. Dominuguez *et al.* [19] showed that γ-alumina gave propylene selectivity more than 80% in a range of reaction temperature 180–240 °C. However, in this study we observed that most of the propanol elimination products over the Pechini alumina were more than 90% acetone. Disordered structure of the Pechini amorphous alumina could result in an imbalanced strength of acid–base sites and the reaction pathway might occur via E_{1cB} proposed by Díez *et al.* The weak physically adsorbing CO_2 site of alumina as shown by the low temperature CO_2 desorption peak in figure 2 could bring about abstraction of α-hydrogen mostly resulting in acetone formation. This might be representative of very poor basicity of alumina surface.

Similar to the pure alumina, the Pechini alumina–zirconia mixed oxides converted to propanol towards acetone with more than 70% selectivity at 150 and 200 °C. Increasing zirconia content in the mixed oxides resulted in a slight decrease in acetone and increase in propylene selectivity at 200 °C. The propylene formation may be ascribed to zirconia. The E_{1cB} mechanism appeared to dominate over the alumina–zirconia mixed oxides. Although the CO_2 desorption peaks of the mixed oxides shifted towards 115 °C, the strength of basicity would not be very effective to abstract β-hydrogen. Increasing propylene selectivity over the alumina–zirconia mixed oxides was probably affected by dual acid–base property of zirconia via the E_2 mechanism. This is in a good agreement with the work reported by Tanabe [29], in which 2-propanol elimination on zirconia catalysts proceed by acid–base site bifunctional catalysis. The orientation of these sites plays an importance role in governing the reaction [30]. However, the orientation of alumina–zirconia mixed oxides structure would be undisciplined resulting in a decrease in acid–base bifunctional property. Therefore, the E_2 mechanism would not dominate over the alumina–zirconia mixed oxides.

Conversion of propanol towards propylene over tetragonal zirconia was observed with more than 80% selectivity at 200 °C. The well-ordered structure of tetragonal zirconia exhibited high selectivity of propylene via the dominant E_2 mechanism. In contrast, partly imperfect crystal of tetragonal zirconia could result in imbalanced acid–base site leading to acetone formation via the E_{1cB} mechanism.

5. Conclusions

The alumina–zirconia mixed oxides produced by the modified Pechini method resulted in combination of aluminium and zirconium atoms. Due to good

dispersion of aluminium and zirconium ions, the mixed oxides present only amorphous form. Apparently, the interaction between Al, Zr, and O in the mixed oxides resulted in higher physical strength of CO_2 adsorption. The modified acidity was, however, ambiguous because all the catalyst samples exhibited low acidity. The imbalance strength of acid–base site due to the imperfect crystal structure of all the catalysts resulted in higher acetone formation via E_{1cB} mechanism. However, 90% propylene selectivity was obtained on pure zirconia prepared by the modified Pechini method and 200 °C reaction temperature.

Acknowledgments

The authors would like to thank the Cooperative Research Network, Thai Ministry of Education, the Thailand Research Fund, the University of New South Wales and CSIRO for financial support. The authors also thank Mr Praharso, Ms Sarah Watson, Mr Richard Burgess and Mr John Starling and Dr Manh Hoang for their support.

References

[1] G. Ertl, H. Knözinger and J. Weitkamp, *Handbook of Heterogeneous Catalysis* (Wiley-VCH, City, 1997).
[2] J.C. Debsikdar, J. Non-Cryst. Solids 86 (1986) 231.
[3] R. Guinebretière, A. Dauger, A. Lecomte and H. Vesteghem, J. Non-Cryst. Solids 147&148 (1992) 542.
[4] J. Livage, F. Beteille, C. Roux, M. Chatry and P. Davidson, Acta mater. 46 (1998) 743.
[5] C. Stöcker and J. Baiker A., Non-Cryst. Solids 223 (1998) 165.
[6] M.M. Pineda, S. Castillo, T. López, R. Gómez, Cordero-Borboa and O. Novaro, Appl. Catal. B: Environ. 21 (1999) 79.
[7] J.L. Lakshmi, T.R.B. Jones, M. Gurgi and J.M. Miller, J. Mol. Catal. A: Chem. 152 (2000) 99.
[8] D.D. Jayaseelan, D.A. Rani, T. Nishikawa, H. Awaji and F.D. Gnanam, J. Euro. Ceram. Soc. 20 (2000) 267.
[9] A.C. Geiculescu and H.J. Rack, J. Non-Crytal. Solids 289 (2001) 53.
[10] Y. Hao, J. Li, X. Yang, X. Wang and L. Lu, Mat. Sci. Eng. A 367 (2004) 243.
[11] M. Ishii, M. Kakihana, K. Ishii, Y. Ikuma and M. Yoshimura, J. Mat. Res. Soc. 11(6) (1996) 1410.
[12] M. Kakihana, S. Kato, M. Yashima and M. Yoshimura, J. Alloys Comp. 280 (1998) 125.
[13] E.N.S. Muccillo, E.C.C. Souza and R. Muccillo, J. Alloys Comp. 344 (2002) 175.
[14] M.P. Pechini, Patent, 11 July (1967) 3,330,697.
[15] C.L. Robert, F. Ansart, C. Deloget, M. Gaudon and A. Rousset, Ceram. Int. 29 (2003) 151.
[16] Y.M. Kong, C.J. Bae, S.H. Lee, H.W. Kim and H.E. Kim, Biomaterials 26 (2005) 509.
[17] I.I. Abu, D.D. Das, H.K. Mishra and A.K. Dalai, J. Colloid Interface Sci. 267 (2003) 382.
[18] R. Mezei and K. Sinkó, Colloid Polym. Sci. 274 (1996) 1054.
[19] J.M. Dominguez, J.L. Hernandez and G. Sandoval, Appl. Cata. A: Gen. 197 (2000) 119.
[20] V.K. Díez, C.R. Apesteguía and J.I. Di Cosimo, J. Catal. 215 (2003) 220.
[21] B.H. Davis, J. Catal. 26 (1972) 348.
[23] P.D.L. Mercera, J.G. van Ommen, E.B.M. Doesburg, A.J. Burggraaf and J.R.H. Ross, Appl. Catal. 71 (1991) 363.
[23] Y. Li, D. He, Z. Cheng, C. Zu, J. Le and Q. Zhu, J. Mol. Catal. A: Chem. 175 (2001) 267.
[24] A. Davydov, *Molecular Spectroscopy of Oxide Catalyst Surfaces* (John Wiley & Sons, England, 2003).
[25] K. Tanabe, M. Misono, Y. Ono and H. Hattari, *New Solid Acids and Bases Their Catalyst Properties* (Kodansha, Tokyo, 1989).
[26] V.K. Díez, C.R. Apesteguía and J.I. Di Cosimo, Catal. Today 63 (2000) 53.
[27] K.C. Waugh, M. Bowker, R.W. Petts, H.D. Vanderwell and J. O'Malley, Appl. Catal. 25 (1986) 121.
[28] A. Gervasini, J. Fenyvesi and A. Auroux, Catal. Lett. 43 (1997) 219.
[29] K. Tanabe, Mat. Chem. Phys. 13 (1985) 347.
[30] S. Chokkaram and B.H. Davis, J. Mol. Catal. A: Chem. 118 (1997) 89.

Available online at www.sciencedirect.com
SCIENCE DIRECT®
Journal of Power Sources 148 (2005) 18–23
JOURNAL OF POWER SOURCES
www.elsevier.com/locate/jpowsour

Short communication

Effects of electrolyte type and flow pattern on performance of methanol-fuelled solid oxide fuel cells

S. Assabumrungrat [a,*], W. Sangtongkitcharoen [a], N. Laosiripojana [b], A. Arpornwichanop [c], S. Charojrochkul [d], P. Praserthdam [a]

[a] *Center of Excellence in Catalysis and Catalytic Reaction Engineering, Department of Chemical Engineering, Faculty of Engineering, Chulalongkorn University, Bangkok 10330, Thailand*
[b] *The Joint Graduate School of Energy and Environment, King Mongkut's University of Technology Thonburi, Bangkok 10140, Thailand*
[c] *Control and Systems Engineering, Department of Chemical Engineering, Faculty of Engineering, Chulalongkorn University, Bangkok 10330, Thailand*
[d] *National Metal and Materials Technology Center (MTEC), Pathumthani, Thailand*

Received 1 November 2004; received in revised form 20 January 2005; accepted 25 January 2005
Available online 2 April 2005

Abstract

A comparison is made of the performances of methanol-fuelled solid oxide fuel cells (SOFCs) with different types of electrolyte (i.e., oxygen ion- and proton-conducting electrolytes) and flow patterns (i.e., plug flow (PF) and mixed flow (MF)). Although it was demonstrated earlier that, under the same inlet steam:methane ratio, an SOFC with a proton-conducting electrolyte (SOFC-H^+) thermodynamically offers higher efficiency than one with an oxygen ion-conducting electrolyte (SOFC-O^{2-}), the benefit of a lower steam requirement for the SOFC-O^{2-} was not taken into account. Therefore, this study attempts to consider the benefit of differences in the steam requirement on the performance of SOFCs operated with different electrolytes and flow patterns. The efficiencies under the best conditions are compared in the temperature range of 900–1300 K. It is found that the maximum efficiencies decrease with increasing temperature and follow the sequence: SOFC-H^+ (PF) > SOFC-O^{2-} (PF) > SOFC-H^+ (MF) > SOFC-O^{2-} (MF). The corresponding inlet H_2O:MeOH ratios are at the carbon formation boundary for the SOFC-O^{2-} electrolyte, but are about 1.3–1.5 times the stoichiometric ratio for the SOFC-H^+. It is clearly demonstrated that the PF mode is superior to the MF mode and that, although the benefit from the lower steam requirement is realized for the SOFC-O^{2-}, the use of the proton-conducting electrolyte in the SOFCs is more promising.

Keywords: Solid oxide fuel cell; Electrolyte; Efficiency; Methanol; Flow pattern; Steam requirement

1. Introduction

The solid oxide fuel cell (SOFC) is a promising technology for electrochemical power generation. Due to its high operating temperature, the SOFC offers the prospect of a wide range of applications, flexibility of fuel choices and the possibility of operation with an internal reformer. Among the various possible fuels, i.e., methane, methanol, ethanol and gasoline, both ethanol and methanol have been reported [1] to offer high electromotive force output and efficiency. Methanol is preferable given its availability, high energy density and ready storage and distribution [2,3], as well as the claim [4] that methanol can be injected directly onto anodes without serious carbon blockage [4]. In operation, the SOFC can use either an oxygen ion-conducting electrolyte or a proton-conducting electrolyte. Most current research efforts have been focusing on the SOFC with the oxygen ion-conducting electrolyte (SOFC-O^{2-}) rather than with the proton-conducting electrolyte (SOFC-H^+). A number of recent studies on advanced SOFC operations, such as development of intermediate temperature-SOFCs [5] and the integration of SOFCs with intercool gas turbines [6], are still based mainly on the use of the oxygen ion-conducting electrolyte.

* Corresponding author. Tel.: +662 218 6868; fax: +662 218 6877.
E-mail address: Suttichai.A@chula.ac.th (S. Assabumrungrat).

0378-7753/$ – see front matter © 2005 Elsevier B.V. All rights reserved.
doi:10.1016/j.jpowsour.2005.01.034

Nomenclature

E	electromotive force of a cell (V)
F	Faraday constant (C mol^{-1})
ΔH^0	lower heating value of methanol (J s^{-1})
K	equilibrium constant of the hydrogen oxidation reaction (kPa$^{-0.5}$)
p_i	partial pressure of component i (kPa)
q	electrical charge (A)
R	gas constant (J mol^{-1} K^{-1})
T	temperature (K)
U_f	fuel utilization (%)
W	electrical work (W)

Greek letters

φ	potential (V)
η	system efficiency (%)

Subscripts

a	anode
c	cathode

Some research efforts have been carried out to compare the performances of SOFCs with different electrolytes. Thermodynamic analysis reveals that the SOFC-H^+ shows higher efficiency for the conversion of chemical energy to electrical power than the SOFC-O^{2-} for systems fed by hydrogen [7]. The same conclusion has also been reached for methane-fuelled SOFCs [8]. The comparisons were, however, performed under the same inlet steam:methane ratio [8]. Our previous work employed thermodynamic analysis to determine the carbon formation boundary for a direct internal-reforming (DIR) SOFC fed by methanol [9] and found that the SOFC-O^{2-} is more attractive than the SOFC-H^+ in terms of a lower steam requirement at the feed to the anode due to the simultaneous formation of steam by the electrochemical reaction of H_2 and O^{2-}.

The difference in the steam requirement among both types of SOFC is particularly pronounced at high values of the extent of the electrochemical reaction. The effect of the SOFC operation modes (i.e., external reforming (ER), indirect internal-reforming (IIR) and direct internal-reforming (DIR)) on the steam requirement at the carbon formation boundary has been investigated for SOFCs fed by methane [10]. It was found that when using the SOFC-O^{2-}, the ER-SOFC and the IIR-SOFC show the same values of the steam:methane ratio at the carbon formation boundary, independent of the extent of electrochemical reaction. By contrast, due to the presence of extra steam from the electrochemical reaction at the anode chamber, the DIR-SOFC can be operated at lower values of the steam:methane ratio compared with the other modes. For the SOFC-H^+, the required steam:methane ratios are higher than those for the SOFC-O^{2-}, but they are independent of the SOFC operation modes. In the performance comparisons among the SOFCs with different types of electrolyte, the differences in the steam requirement should be taken into account as it is generally known that extra steam can act as a diluent and lower the SOFC efficiency. Therefore, it remains unclear whether the SOFC-H^+ is superior to the SOFC-O^{2-}.

It is the objective of this study to compare the performances of DIR-SOFCs with different electrolytes (i.e., oxygen ion- and proton-conducting electrolytes) and flow patterns (i.e., plug flow (PF) and mixed flow (MF)) by taking into account the benefit from the differences in their steam requirement. The flow pattern should be considered because it affects both the steam requirement of the system, particularly for the SOFC-O^{2-}, and the cell performance. The information obtained from this work is important for determining whether research into fuel cell development should be directed towards the system using the proton-conducting electrolyte.

2. Theory

The reactions involved in the production of hydrogen from methanol steam-reforming can be represented by Eqs. (1)–(3) [11,12], i.e.,

$$CH_3OH = 2H_2 + CO \text{ (methanol decomposition)} \quad (1)$$

$$CO + H_2O = H_2 + CO_2 \text{ (water gas shift reaction)} \quad (2)$$

$$CO + 3H_2 = CH_4 + H_2O \text{ (methanation)} \quad (3)$$

The reactions taking place at the anode and the cathode for the two types of electrolyte can be summarized as follows:

SOFC-O^{2-}:

$$\text{anode} : H_2 + O^{2-} = H_2O + 2e^- \quad (4)$$

$$\text{cathode} : O_2 + 4e^- = 2O^{2-} \quad (5)$$

SOFC-H^+:

$$\text{anode} : H_2 = 2H^+ + 2e^- \quad (6)$$

$$\text{Cathode} : 2H^+ + \tfrac{1}{2}O_2 + 2e^- = H_2O \quad (7)$$

As seen from the above equations, it should be noted that water is produced in the anode chamber for the SOFC-O^{2-}, but in the cathode chamber for the SOFC-H^+.

The electromotive force (E) of a cell is the difference in the potential of the two electrodes. Thus, the electromotive force can be represented as follows:

$$E = |\varphi_c - \varphi_a| \quad (8)$$

where φ_c and φ_a are the potentials of the cathode and the anode, respectively. The electrode potential can be calculated from Nernst equation. Because the electrochemical reactions at the electrodes are different, depending on the electrolyte

type, the potential can be expressed as follows:

$$\text{SOFC-O}^{2-}: \quad \varphi = \left(\frac{RT}{4F}\right) \ln\, p_{O_2} \tag{9}$$

$$\text{SOFC-H}^{+}: \quad \varphi = \left(\frac{RT}{2F}\right) \ln\, p_{H_2} \tag{10}$$

where p_i is the partial pressure of component i, R the universal gas constant, T the absolute temperature and F is the Faraday constant.

For SOFC-O^{2-}, the partial pressure of oxygen in the cathode chamber is calculated from its mole fraction, while the following equation is used to determine the partial pressure of oxygen in the anode chamber.

$$p_{O_2} = \left(\frac{p_{H_2O}}{K p_{H_2}}\right)^2 \tag{11}$$

For the SOFC-H^{+}, the partial pressure of hydrogen in the anode chamber is calculated from its mole fraction, while the partial pressure of hydrogen in the cathode is given by:

$$p_{H_2} = \frac{p_{H_2O}}{K p_{O_2}^{1/2}} \tag{12}$$

In Eqs. (11) and (12), K is the equilibrium constant of the hydrogen oxidation reaction.

Regarding the possible SOFC configurations, gas flow within the flow channels of the SOFC stack can be classified broadly into two ideal flow patterns, i.e., plug flow and mixed flow. The former is characterized by the fact that the gas mixture moves orderly through the channel with no element of the gas mixing with any other element ahead or behind, whereas with mixed flow the contents are well-mixed and uniform throughout. Although most typical SOFCs are operated under a condition close to the PF mode, the MF mode can be realized by using a high recycle rate.

In the PF mode, the electromotive force (E) changes along the SOFC stack due to the distribution of gas compositions along the flow channels in both the anode and the cathode sections. The average electromotive force ($\bar{E}$) can be obtained from numerical integration of the gas distribution along the stack. To simplify the calculation, the gas compositions at the anode are assumed to reach their equilibrium compositions along the stack. The calculation procedures of the equilibrium compositions in SOFCs have been described in our previous work [9].

When current is drawn from the SOFC cell, the maximum electrical work (W) produced by the SOFC and the system efficiency (η) defined as the ratio of the maximum conversion of the chemical energy of the fuel fed in the SOFC system to electrical work, are calculated from Eqs. (13) and (14), respectively.

$$W = q\bar{E} \tag{13}$$

$$\eta = \frac{q\bar{E}}{-\Delta H^0} \times 100\% \tag{14}$$

where q is the electrical charge passing through the electrolyte and ΔH^0 is the lower heating value (LHV) of methanol at the standard condition.

It should be noted that the assumption of the equilibrium state of gas compositions along the flow channel may be reasonable because the rates of methanol steam-reforming and the water gas shift reaction are fast, particularly at high temperature [13–16]. Several researchers reported that the conversion of methanol from the methanol steam-reforming always close to 100% when the operating temperature above 573 K is applied [13–15]. Moreover, at 1173 K, methanol steam-reforming has been reported [16] to occur homogenously and reach equilibrium. Deviation from this equilibrium condition would result in lower values of the electromotive force and the efficiency of SOFCs as less hydrogen would be generated in the anode chamber to compensate for the hydrogen consumed by the electrochemical reaction. Therefore, the results shown in this work represent the best performances for all SOFC cases.

3. Results and discussion

The efficiency and electromotive force at different fuel utilizations for methanol-fuelled SOFCs with different electrolyte types and flow patterns are shown in Fig. 1. The inlet steam:methanol (H_2O:MeOH) ratio is at the stoichiometric value of 1 for all SOFCs. The fuel utilization, U_f, is defined as the moles of hydrogen consumed by the electrochemical reaction divided by the maximum moles of hydrogen produced from the methanol steam-reforming (3 mol of hydrogen per 1 mol of methanol). As can be seen from Fig. 1(a), efficiencies increase with increasing fuel utilization for all SOFCs because more hydrogen is utilized for electrical power production. At high fuel utilization, however, the efficiencies of the SOFCs with the MF mode decrease, which corresponds to a sharp drop in the electromotive force observed in the MF mode (Fig. 1(b)). Although it is typical that the electromotive force decreases with increasing fuel utilization as the hydrogen partial pressure becomes smaller at higher fuel utilization, the flow characteristics of the PF mode allow the electromotive force to decrease gradually along the flow channel. Consequently, the PF mode provides a higher average electromotive force than the MF mode in which the electromotive force is at its minimum value over the entire cell area. It should be noted that although both ideal flow modes are not achieved in real operations, experimental SOFCs using tubular and planar cells show behaviour close to the PF and MF modes, respectively.

At present, most experimental studies related to the investigation of SOFC performance are based on systems that use an oxygen ion-conducting electrolyte, and experimental comparison of SOFC performance for the two flow patterns at the same operating condition is not available in the literature. According to Veyo and Forbes [17], an efficiency of 66–70% was achieved at 85% fuel utilization when pure hy-

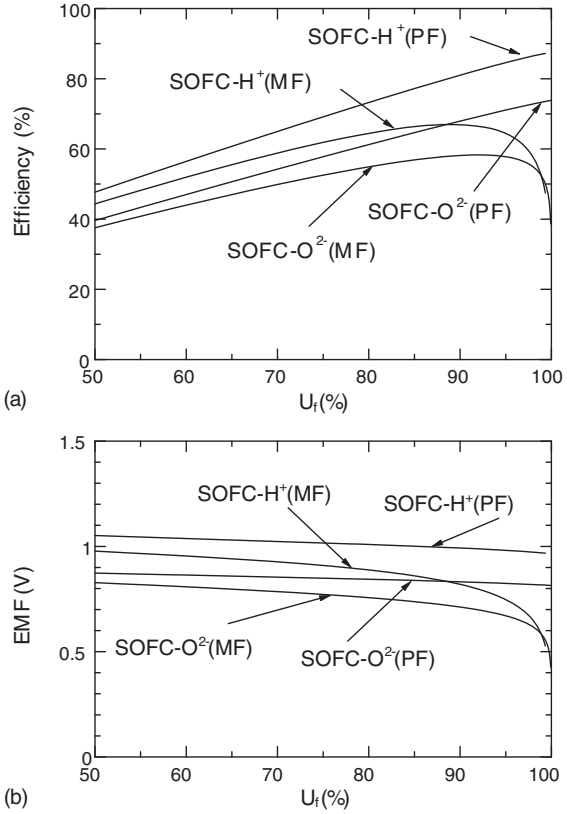

Fig. 1. Performance of SOFC-O^{2-} and SOFC-H^{+} operated under plug flow (PF) and mixed flow (MF): (a) efficiency; (b) electromotive force (inlet H_2O:MeOH = 1, T = 1300 K, P = 101.3 kPa).

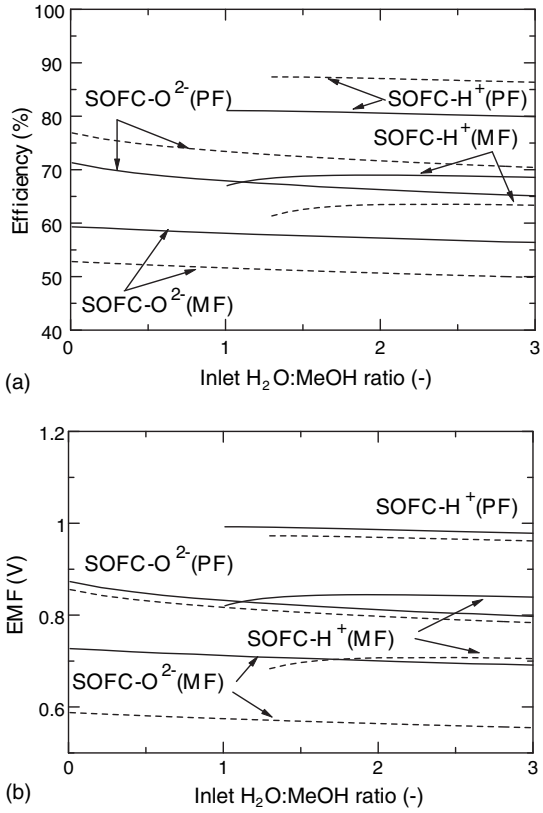

Fig. 2. Influence of inlet H_2O:MeOH ratio on SOFC performance at fuel utilization of 90% (solid line) and 99% (dashed line): (a) efficiency; (b) electromotive force (T = 1300 K, P = 101.3 kPa).

drogen was used as a fuel in a tubular SOFC. At the same level of utilization, the data in Fig. 1(a) show that the efficiency is reduced to 65% if methanol is fed to the system and a SOFC-O^{2-} (PF) combination is used. The information obtained has strengthened the fact that operation with pure hydrogen fuel yields higher efficiency than using any fuel of an equivalent amount. In addition, when methane was fed to a planar SOFC, at a methane utilization of 86% an efficiency of 53.6% was obtained [18], which is close to the value of 55% if methanol is applied in place of methane in our study (SOFC-O^{2-} (MF)).

The results in Fig. 1 also show that the SOFC-H^{+} offers higher efficiency than the SOFC-O^{2-} for both flow pattern modes. This is in good agreement with previous results obtained for SOFCs fuelled by hydrogen [7] and methane [8]. The electrolyte type plays an important role on the value of the hydrogen partial pressure in the anode side and, therefore, on the electromotive force and efficiency of the SOFC. The partial pressure of hydrogen for the SOFC-H^{+} is relatively higher than that for the SOFC-O^{2-} because the water generated from the electrochemical reaction is present and acts as an inert gas at the anode side for the SOFC-O^{2-}, whereas it appears at the cathode side for the SOFC-H^{+}. It is noted that when pure hydrogen is fed to the anode, the mole fraction of hydrogen in the anode chamber is always unity along the cell length for the SOFC-H^{+}.

According to the above analysis for SOFCs with different electrolyte types and flow patterns under the same inlet H_2O:MeOH ratio, it is demonstrated that the SOFC with the proton-conducting electrolyte operated under the PF mode (SOFC-H^{+} (PF)) is the most favourable choice. Our previous work [9] has shown, however, that the steam requirement to operate the SOFC without carbon formation for the SOFC-O^{2-} is lower than that of the SOFC-H^{+}. Thus, it is important to take into account this benefit in efficiency comparisons between different SOFCs. The effect of the inlet H_2O:MeOH ratio on the efficiency and electromotive force of the SOFC at the fuel utilizations of 90% (solid lines) and 99% (dashed lines) is presented in Fig. 2. The minimum inlet H_2O:MeOH ratios represent values at the carbon formation boundary. Details of the calculations for the carbon formation boundary in each operating mode have been described in our earlier work [9]. It was found that the SOFC-O^{2-} can be operated at the carbon-free condition without a requirement for extra steam in the methanol feed, and both the efficiency and electromotive force decrease with an increase in the inlet H_2O:MeOH ratio. Therefore, an addition of steam in the feed lowers the performance of the SOFC-O^{2-}. For the SOFC-H^{+}, the inlet H_2O:MeOH ratios at the carbon formation boundary are higher than those for the SOFC-O^{2-}, particularly at high fuel utilization, and the effect of the inlet H_2O:MeOH ratio on the SOFC performance is less pronounced. As the water from

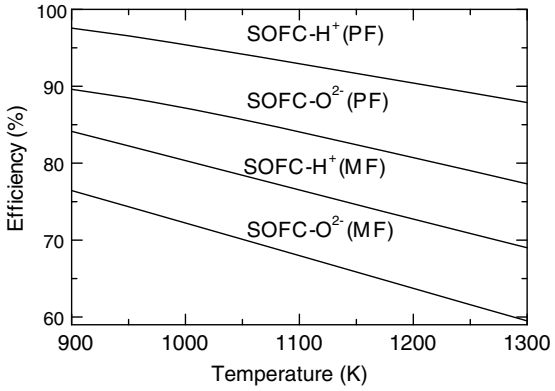

Fig. 3. Maximum efficiency of different SOFCs at different operating temperatures ($P = 101.3$ kPa).

the electrochemical reaction is generated at the cathode side, additional steam is required in the methanol feed at the anode side to promote hydrogen production. On the other hand, excessive steam will reduce the hydrogen concentration of the gas mixture at the anode side.

As it has been found that the SOFC performance is dependent on fuel utilization and inlet H_2O:MeOH ratio, it is possible to determine the maximum efficiency and the corresponding conditions for all SOFC cases at a specified temperature by performing calculations at various values of the inlet H_2O:MeOH ratio and the fuel utilization. The results for a temperature range of 900–1300 K are shown in Figs. 3 and 4. The maximum efficiencies follow the sequence: SOFC-H^+ (PF) > SOFC-O^{2-} (PF) > SOFC-H^+ (MF) > SOFC-O^{2-} (MF). The corresponding inlet H_2O:MeOH ratios are at the carbon formation boundary for both the SOFC-O^{2-} (PF) and SOFC-O^{2-} (MF), but are about 1.3 and 1.5 times the stoichiometric ratio for the SOFC-H^+ (MF) and the SOFC-H^+ (PF), respectively. The values of fuel utilization at the maximum efficiency are mainly governed by the flow pattern. For SOFCs operated under the PF mode, the utilization is constant at approximately 99%, but decreases slightly from 96.1 to 92.3% and from 95.5 to 92.0% for the SOFC-H^+ (MF) and the SOFC-O^{2-} (MF), respectively, when the temperature is increased from 900 to 1300 K. From these results, it is obvious that the proton-conducting electrolyte is more preferable for use in SOFCs. In addition, the PF mode is better than the MF mode. The SOFC-H^+ provides approximately 7.7–10.6% higher efficiency than the SOFC-O^{2-} with the same flow pattern mode in the range of temperature studied. The maximum efficiency for all cases decreases with increasing temperature. This is in good agreement with the decrease in electromotive force due to the thermodynamic Gibb's free energy.

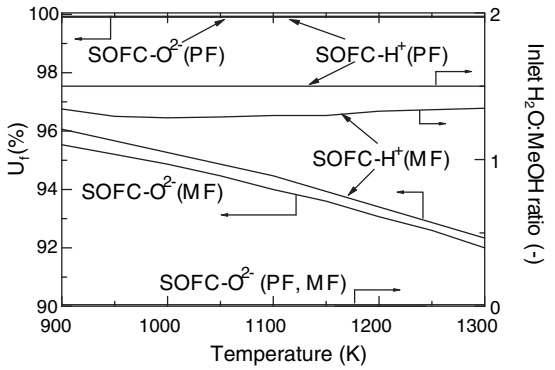

Fig. 4. Operating conditions corresponding to those in Fig. 3, at maximum efficiency ($P = 101.3$ kPa).

From the above studies, it is found that although the benefit of lower steam requirement is taken into account in the calculations for the SOFC-O^{2-}, the SOFC-H^+ still shows higher efficiency than the SOFC-O^{2-} for both the PF and the MF modes. This implies that the development of SOFCs should be directed towards the use of the proton-conducting electrolyte. It should also be noted, however, that this study has not taken into account all the losses presented in real SOFC operation and, therefore, it will be the aim of our next investigation to consider these losses when undertaking efficiency comparisons. The SOFC-H^+ allows the cell to reach easily a high hydrogen utilization without an additional effort to separate steam from the anode gas and circulate it back to the cell as required for the SOFC-O^{2-}.

4. Conclusions

The performance of methanol-fuelled SOFCs using proton- and oxygen ion-conducting electrolytes and operating under plug flow and mixed flow modes is investigated. The electromotive force and efficiency are dependent on fuel utilization, inlet H_2O:MeOH ratio, operating temperature, operation mode and electrolyte type. The benefit of less steam requirement for the SOFC-O^{2-} is taken into account in comparisons of SOFC performance. It is demonstrated that the plug flow is superior to the mixed flow and that the use of the proton-conducting electrolyte is more preferable. These findings indicate that SOFC development should be directed towards a system that was the proton-conducting electrolyte.

Acknowledgements

Support from the Thailand Research Fund and Chulalongkorn University Graduate Scholarship commemorating the 72nd Anniversary of H.M. King RAMA IX is gratefully acknowledged.

References

[1] S.L. Douvartzides, F.A. Coutelieris, K. Demin, P.E. Tsiakaras, AIChE J. 49 (2003) 248–257.
[2] B. Emonts, J.B. Hansen, S.L. Jorgensen, B. Hohlein, R. Peters, J. Power Sources 71 (1998) 288.

[3] K. Ledjeff-Hey, V. Formanski, T. Kalk, J. Roes, J. Power Sources 71 (1998) 199–207.
[4] G.J. Saunders, J. Preece, K. Kendal, J. Power Sources 131 (1–2) (2004) 23–26.
[5] P. Aguiar, C.S. Adjiman, N.P. Brandon, J. Power Sources 138 (2004) 120–136.
[6] Y. Yi, A.D. Rao, J. Brouwer, G.S. Samuelsen, J. Power Sources 132 (2004) 77–85.
[7] A.K. Demin, P.E. Tsiakaras, Int. J. Hydrogen Energy 26 (2001) 1103–1108.
[8] A.K. Demin, P.E. Tsiakaras, V.A. Sobyanin, S.Y. Hramova, Solid State Ionics 152–153 (2002) 555–560.
[9] S. Assabumrungrat, N. Laosiripojana, V. Pavarajarn, W. Sangtongkitcharoen, A. Tangjitmatee, P. Praserthdam, J. Power Sources 139 (2005) 55–60.
[10] W. Sangtongkitcharoen, S. Assabumrungrat, V. Pavarajarn, N. Laosiripojana, P. Praserthdam, J. Power Sources 142 (2005) 75–80.
[11] J.C. Amphlett, M.J. Evans, R.A. Jones, R.F. Mann, R.D. Weir, Can. J. Chem. Eng. 59 (1981) 720.
[12] Y. Lwin, W.R.W. Daud, A.B. Mohamad, Z. Yaakob, Int. J. Hydrogen Energy 25 (1) (2000) 47–53.
[13] P.J. de Wild, M.J.F.M. Verhaak, Catal. Today 60 (2000) 3–10.
[14] X. Zhang, P. Shi, J. Mol. Catal. A-Chem. 194 (2003) 99–105.
[15] P. Chantaravitoon, S. Chavadej, J. Schwank, Chem. Eng. J. 97 (2004) 161–171.
[16] N. Laosiripojana, Reaction engineering of indirect internal steam reforming of methane for application in solid oxide fuel cells, Ph.D. Thesis, University of London, UK, 2003.
[17] S.E. Veyo, C.A. Forbes, in: P. Stevens (Ed.), Proceedings of Third European Solid Oxide Fuel Cell Forum, Nantes, France, 1998, pp. 79–86.
[18] Y. Matsuzaki, Y. Baba, T. Ogiwara, H. Yakabe, in: J. Huijsmans (Ed.), Proceedings of Fifth European Solid Oxide Fuel Cell Forum, Lucerne, Switzerland, 2002, pp. 776–783.

Catalysis Letters Vol. 103, Nos. 1–2, September 2005 (© 2005)
DOI: 10.1007/s10562-005-6502-x

Synthesis, characterization, and catalytic properties of Pd and Pd–Ag catalysts supported on nanocrystalline TiO_2 prepared by the solvothermal method

Joongjai Panpranot[a,*], Lakkana Nakkararuang[a], Bongkot Ngamsom[b], and Piyasan Praserthdam[a]

[a]*Department of Chemical Engineering, Center of Excellence on Catalysis and Catalytic Reaction Engineering, Chulalongkorn University, Bangkok, 10330, Thailand*

[b]*Department of Chemical Engineering, King Mongkut Institute of Technology, Ladkrabang, Bangkok, Thailand*

Received 25 February 2005; accepted 5 May 2005

Nanocrystalline titania have been prepared by thermal decomposition of titanium (IV) *n*-butoxide in two different solvents (toluene and 1,4-butanediol) at 320 °C and employed as supports for Pd and Pd–Ag catalysts for selective acetylene hydrogenation for the first time. The titania products obtained from both solvents were pure anatase phase with relatively the same crystallite sizes and BET surface areas. However, due to different crystallization pathways, the number of Ti^{3+} defective sites as shown by ESR results of the titania prepared in toluene was much higher than the ones prepared in 1,4-butanediol. It was found that the use of anatase titania with higher defective sites as a support for Pd catalysts resulted in lower activity and selectivity in selective acetylene hydrogenation. However, this effect was suppressed by Ag promotion.

KEY WORDS: nanocrystalline titania; solvothermal method; acetylene hydrogenation; supported Pd catalysts.

1. Introduction

The solvothermal method has been used to successfully synthesize various types of nanosized metal oxides with large surface area, high crystallinity, and high thermal stability [1–7]. For example, thermal decomposition of titanium (IV) *n*-butoxide in organic solvents yields nano-sized pure anatase titania without bothersome procedures such as purification of the reactants or handling in an inert atmosphere. These nanocrystalline titanias have been shown to exhibit high photocatalytic activities [8, 9]. However, the thermal stability as well as photocatalytic activity of the solvothermal-derived titania were found to be strongly dependent on the organic solvent used as the reaction medium during crystallization [7]. The titania products synthesized in toluene showed lower thermal stability and lower photocatalytic activities than the ones synthesized in 1,4-butanediol. The authors suggested that the amount of defect structures in the titania prepared by this method was different depending on the solvent used due to the different crystallization pathways.

Due to their unique properties, it is interesting to investigate the characteristics and catalytic properties of the solvothermal-derived nanocrystalline titania supported noble metal as another exploitation of such materials. It is well known that metal catalyst supported on titania exhibits 'the strong metal-support interaction' (SMSI) phenomenon after reduction at high temperatures due to the decoration of the metal surface by partially reducible metal oxides [10, 11] or by an electron transfer between the support and the metals [12, 13]. In selective hydrogenation of acetylene to ethylene on Pd/TiO_2 catalysts, the charge transfer from Ti species to Pd weakened the adsorption strength of ethylene on the Pd surface hence higher ethylene selectivity was obtained [14].

In this study, nanocrystalline titanias were synthesized by the solvothermal method in two different solvents (1,4-butanediol and toluene) and employed as supports for Pd and Pd–Ag catalysts for selective hydrogenation of acetylene for the first time. The physicochemical properties of the titania and the titania supported catalysts were analyzed by means of X-ray diffraction (XRD), N_2 physisorption, scanning electron microscopy (SEM), electron spin resonance (ESR), and CO chemisorption. Moreover, the effect of defective structures in titania on the catalytic performance of the titania supported Pd and Pd–Ag catalysts in acetylene hydrogenation was investigated.

2. Experimental

2.1. Preparation of TiO_2 by the solvothermal method

TiO_2 was prepared according to the method described in Payakgul *et al.* [7] using 25 g of titanium(IV) *n*-butoxide (TNB) 97% from Aldrich. The starting material was suspended in 100 ml of solvent

* To whom correspondence should be addressed.
E-mail: joongjai.p@eng.chula.ac.th

1011-372X/05/0900-0053/0 © 2005 Springer Science+Business Media, Inc.

(1,4-butanediol or toluene) in a test tube and then set up in an autoclave. In the gap between the test tube and autoclave wall, 30 ml of solvent was added. After the autoclave was completely purged with nitrogen, the autoclave was heated to 320 °C at 2.5 °C/min and held at that temperature for 6 h. Autogenous pressure during the reaction gradually increased as the temperature was raised. After the reaction, the autoclave was cooled to room temperature. The resulting powders were collected after repeated washing with methanol by centrifugation. They were then air-dried at room temperature.

2.2. Preparation of TiO_2 supported Pd and Pd–Ag catalysts

1%Pd/TiO_2 were prepared by the incipient wetness impregnation technique using an aqueous solution of the desired amount of $Pd(NO_3)_2$ (Wako). The catalysts were dried overnight at 110 °C and then calcined in N_2 flow 60 cc/min with a heating rate of 10 °C/min until the temperature reached 500 °C and then in air flow 100 cc/min at 500 °C for 2 h. 1%Pd–3%Ag/TiO_2 catalysts were prepared by sequential impregnation of the 1%Pd/TiO_2 with an aqueous solution of $Ag(NO_3)$ (Aldrich) and were calcined using the same calcination procedure as for 1%Pd/TiO_2.

2.3. Catalyst characterization

The BET surface areas of the samples were determined by N_2 physisorption using a Micromeritics ASAP 2000 automated system. Each sample was degassed under vacuum at $< 10\mu$m Hg in the Micromeritics ASAP 2000 at 150 °C for 4 h prior to N_2 physisorption. The XRD spectra of the catalyst samples were measured from 20–80° 2θ using a SIEMENS D5000 X-ray diffractometer and CuK_α radiation with a Ni filter. Electron spin resonance (ESR) spectra were taken at −150 °C using a JEOL JES-RE2X spectrometer. Relative percentages of palladium dispersion were determined by pulsing carbon monoxide over the reduced catalyst. Approximately 0.2 g of catalyst was placed in a quartz tube in a temperature-controlled oven. CO adsorption was determined by a thermal conductivity detector (TCD) at the exit. Prior to chemisorption, the catalyst was reduced in a flow of hydrogen (50 cc/min) at room temperature for 2 h. Then the sample was purged at this temperature with helium for 1 h. Carbon monoxide was pulsed at room temperature over the reduced catalyst until the TCD signal from a pulse was constant.

The ethylene-TPD profiles of supported palladium catalysts were obtained by temperature programmed desorption from 35 to 800 °C. Approximately 0.05 g of a calcined catalyst was placed in a quartz tube in a temperature-controlled oven and connected to a thermal conductivity detector (TCD). The catalyst was first reduced in H_2 flow 100 cc/min for 1 h at 500 °C (using a ramp rate of 10 °C/min) and cooled down to room temperature before ramping up again to 70 °C in helium flow. The catalyst surface was saturated with ethylene by applying a high purity grade ethylene from the Thai Industrial Gas, Co., Ltd. at 60 ml/min for 3 h. Then the samples were flushed with helium while cooling down to room temperature for about 1 h. The temperature-programmed desorption was performed with a constant heating rate of ca. 10 °C/min from 35 to 800 °C. The amount of desorbed ethylene was measured by analyzing the effluent gas with a thermal conductivity detector.

2.4. Selective hydrogenation of acetylene

Approximately 0.2 g of catalyst was packed in a quartz tubular reactor in a temperature-controlled furnace. Prior to reaction, the catalyst was reduced in H_2 at 500 °C for 2 h. The reactor was then cooled down to 40 °C and the reactant gas composed of $C_2H_2/H_2 = 1{:}2$ (2/4 cc) balance with N_2 total flow of 200 ml/min was fed to the reactor to start the reaction. The product samples were taken at 30 min intervals and analyzed by GC.

3. Results and discussion

3.1. Physicochemical properties of the solvothermal-derived TiO_2

Figure 1 shows the XRD patterns of the TiO_2 particles prepared by thermal decomposition of titanium *n*-butoxide in organic solvents. It was found that nano-sized anatase titania was produced without any contamination of other phases. The crystallite sizes (d) and BET surface areas of the TiO_2 products synthesized in 1,4-butanediol and toluene were found to be essentially the same ($d = 9$–10 nm and BET S.A. 65 m^2/g). However, the morphology of the TiO_2 particles was different as shown by SEM micrographs (figure 2). The products synthesized in toluene agglomerated into spherical micron-sized particles whereas irregular aggregates of nanometer particles were observed for the ones prepared in 1,4-butanediol. The effect of reaction medium on the synthesis of TiO_2 nanocrystals by solvothermal method has recently been reported by Praserthdam *et al.* [7]. It was suggested that anatase titania synthesized in 1,4-butanediol was the result from direct crystallization while titania synthesized in toluene was transformed from precipitated amorphous intermediate.

Due to the different crystallization pathways, degree of crystallinity of the TiO_2 synthesized in 1,4-butanediol and toluene may be different. In this study, the number of defective sites of TiO_2 was determined using electron spin resonance spectroscopy technique and the results are shown in figure 3. ESR has been shown to be a powerful tool to detect Ti^{3+} species in TiO_2 particles. Such Ti^{3+} species are produced by trapping of electrons at defective sites of TiO_2 and the amount of

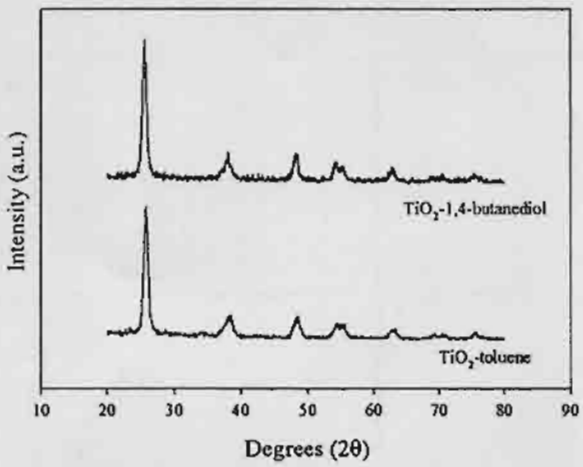

Figure 1. XRD patterns of the solvothermal-derived TiO_2 prepared in two different solvents.

accumulated electrons may therefore reflect the number of defective sites [15]. The signal of g value less than 2 was assigned to Ti^{3+} ($3d^1$) [16]. Both TiO_2-1,4-butanediol and TiO_2-toluene show Ti^{3+} ESR signal at $g = 1.9979–1.9980$ with TiO_2-toluene exhibited much higher intensity. The results clearly show that TiO_2-toluene possessed more Ti^{3+} defective sites than TiO_2-1,4-butanediol.

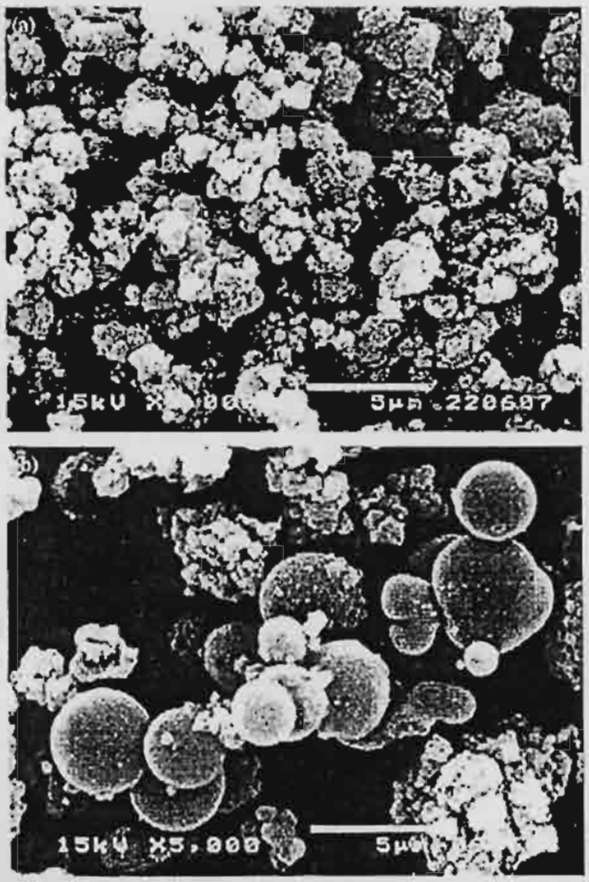

Figure 2. SEM micrographs of (a) TiO_2-1,4-butanediol and (b) TiO_2-toluene.

3.2. *Characteristics of Pd/TiO_2 and Pd–Ag/TiO_2 catalysts*

Table 1 shows the physicochemical properties of the Pd/TiO_2 and Pd–Ag/TiO_2 catalysts. It was found that BET surface areas of the TiO_2 were slightly decreased after impregnation Pd and Pd–Ag suggesting that the metals were deposited in some of the pores of TiO_2. The pulse CO chemisorption technique was based on the assumption that one carbon monoxide molecule adsorbs on one palladium site [17–19]. It was found that Pd/TiO_2-1,4-butanediol exhibited higher amount of CO chemisorption than Pd/TiO_2-toluene. Since both TiO_2 supports possess similar BET surface areas and crystallite sizes, the differences in the amount of active surface Pd were probably induced by the different degrees of crystallinity of the TiO_2 particles.

Addition of Ag to Pd/TiO_2 catalysts resulted in lower amount of active surface Pd. The bimetallic Pd–Ag catalyst has been reported to show many beneficial effects in selective hydrogenation of acetylene to ethylene, for examples, suppression of oligomers formation and improvement of ethylene selectivity [20]. These beneficial effects are due to the altered surface arrangement of Ag atoms on the Pd surface. Roder *et al.* [21] suggested that Ag atoms are likely to stay at the surface in segregated form with Pd rather than forming an alloy.

3.3. *Catalytic performance in selective acetylene hydrogenation*

The conversion and selectivity of Pd and Pd–Ag catalysts supported on TiO_2-1,4-butanediol and TiO_2-toluene in selective acetylene hydrogenation as a function

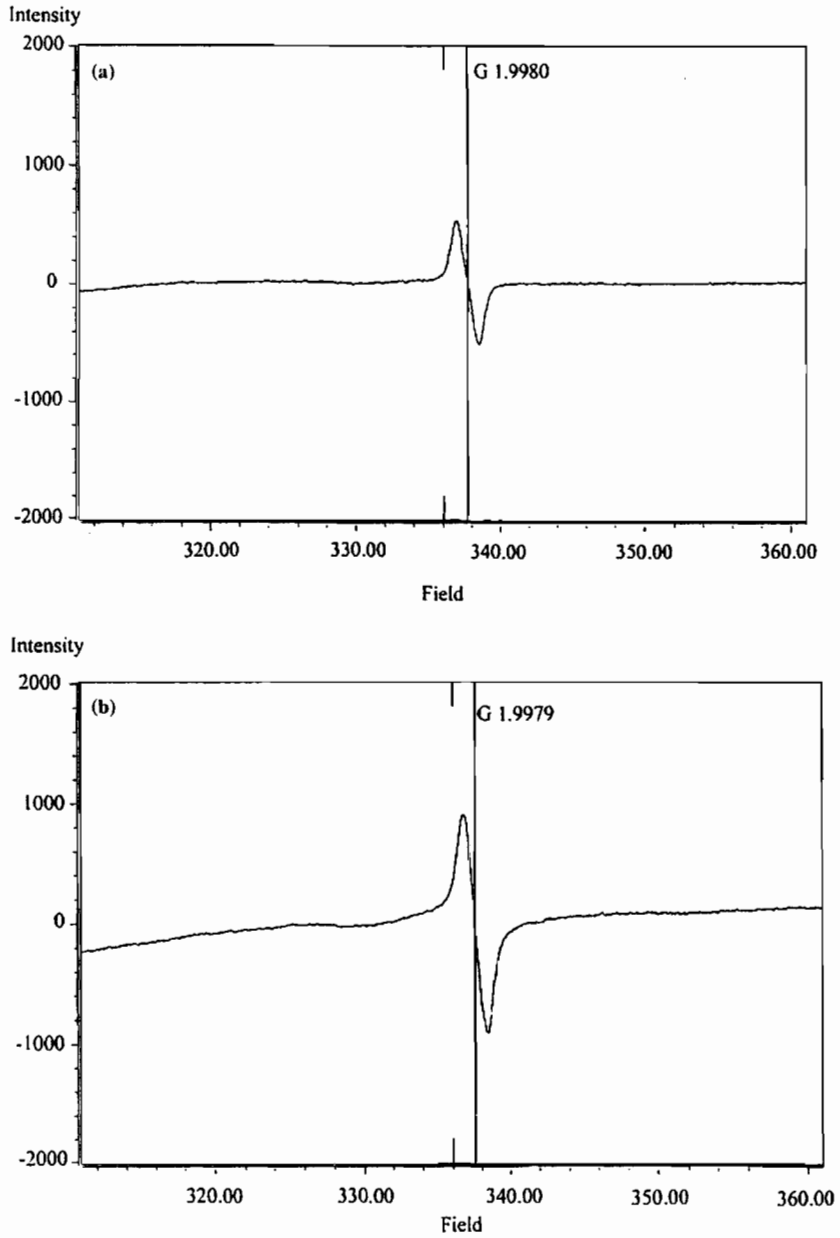

Figure 3. ESR results of (a) TiO_2-1,4-butanediol and (b) TiO_2-toluene.

Table 1
Characteristics of Pd and Pd–Ag catalysts supported on solvothermal-derived TiO_2 prepared in different solvents

Catalyst	BET S.A.[a] (m^2/g)	CO chemisorption[b] (molecule CO $\times 10^{18}$/g catalysis)	Pd dispersion (%)	d_p, Pd^0 (nm)[c]
1%Pd/TiO_2 (1,4-butanediol)	52	5.65	10.0	11.2
1%Pd/TiO_2 (toluene)	60	4.69	8.3	13.5
1%Pd–3%Ag/TiO_2 (1,4-butanediol)	42	2.18	3.8	29.1
1%Pd–3%Ag/TiO_2 (toluene)	47	2.05	3.6	30.9

[a]Error of measurement = ± 10 %.
[b]Error of measurement = ± 5 %.
[c]Based on $d = 1.12/D$ (nm), where D = fractional metal dispersion [17].

of reaction temperature are shown in figures 4 and 5, respectively. The use of TiO_2-1,4-butanediol as the supports for Pd or Pd–Ag catalysts resulted in higher acetylene conversions than the ones supported on TiO_2-toluene. Acetylene conversion of the single metal catalysts reached 100% at ca. 70 °C while those for the bimetallic catalysts showed only 40% (for Pd–Ag/TiO_2-toluene) and 80% (for Pd–Ag/TiO_2-1,4-butanediol) conversions at 90 °C. The ethylene selectivity for all the catalysts at the temperature ranges 40–50 °C were not significantly difference and were found to be ca. 80–90%. However, at 60–70 °C, ethylene selectivity of Pd/TiO_2-1,4-butanediol was much higher than those of Pd/TiO_2-toluene. Ethylene selectivity for the Ag-promoted catalysts were similar for all the reaction temperature used in this study and were higher than those of the non-promoted ones. It was reported that SMSI effect occurs for Pd/TiO_2 catalysts after reduction at high temperature lowering the adsorption strength of ethylene on catalyst surface thus high ethylene selectivity is obtained [10]. Recently, Fan *et al.* [22] reported that diffusion of Ti^{3+} from the lattice of anatase TiO_2 to surface Pd particle can lower the temperature to induce SMSI. However, in this study we have found that use of TiO_2 with higher concentration of Ti^{3+} as a support for Pd catalyst resulted in lower acetylene conversion and selectivity for ethylene after reduction at 500 °C. The turnover frequencies were calculated to be ca. 0.50–0.95 s^{-1} based on the reaction rates at 50 °C. Since the TOFs for all the catalysts were quite similar, it would appear that there was no support effect on the specific activity.

The characteristics of the surface active sites of the catalysts were studied by means of the temperature programmed desorption of ethylene from 30–800 °C. The results are shown in figure 6. The TiO_2-toluene support was found to exhibit two main desorption peaks at ca. 460–680 °C while the TiO_2-1,4-butanediol showed only one desorption peak at 680°C. The results suggest that there were two different active sites on the TiO_2-toluene support, probably Ti^{3+} and Ti^{4+} sites. The high temperature peak for both TiO_2 supports disappeared after Pd loading as shown in the profiles of the Pd catalysts. However, desorption peak at ca. 460 °C was still apparent for Pd/TiO_2-toluene. Since lower ethylene

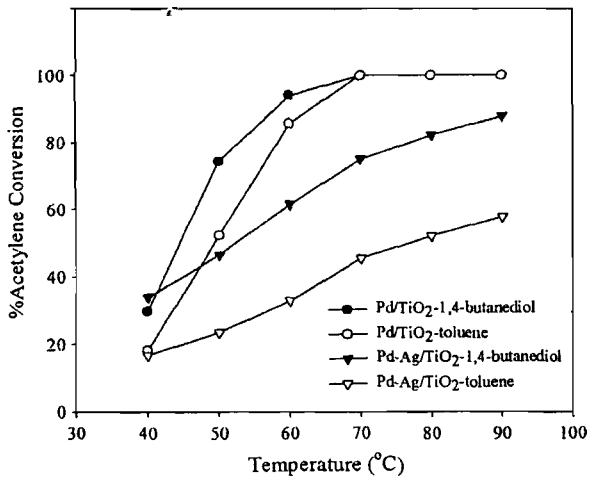

Figure 4. Acetylene conversion as a function of temperature for various TiO_2 supported catalysts.

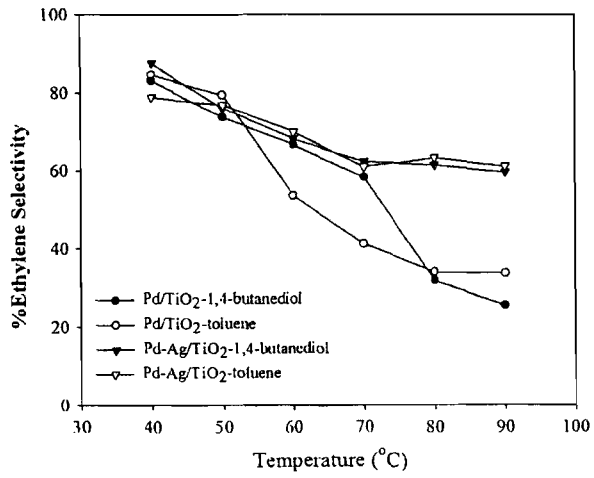

Figure 5. Ethylene selectivity as a function of temperature for various TiO_2 supported catalysts.

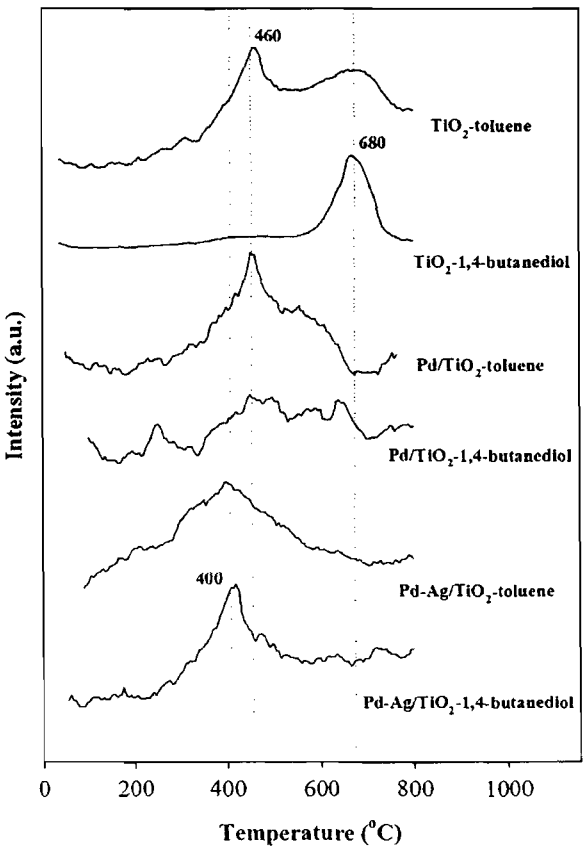

Figure 6. Ethylene-TPD results.

selectivity was found for Pd/TiO_2-toluene than Pd/TiO_2-1,4-butanediol for similar acetylene conversion, this peak can be assigned to the sites for ethylene hydrogenation to ethane. Ethylene hydrogenation is usually believed to take place on the support by means of a hydrogen transfer mechanism [23]. Since only Ti^{3+} species that were in contact with palladium surface promoted SMSI effect [22], ethylene hydrogenation could take place on the Ti^{3+} defective sites that were not in contact with palladium resulting in lower acetylene conversion and selectivity for ethylene as observed in the case of Pd/TiO_2-toluene in this study. The Ag-promoted Pd catalysts exhibited only one ethylene desorption peak at ca. 400 °C suggesting that the Pd catalyst surface on both TiO_2 supports was modified by Ag atoms. The presence of Ag probably blocked the sites for ethylene hydrogenation to ethane for both catalysts thus a significant improvement in ethylene selectivity was observed especially for high acetylene conversion at high temperature. Further study on the titanium defective sites using more sophisticated characterization techniques such as XPS and SIMS is recommended in order to obtain more information on other titanium oxidation states that might be involved in the defective sites, oxygen to titanium ratio, etc. However, in term of catalyst deactivation, we did not observe a decrease in activity or ethylene selectivity for all the catalyst after 12 h on stream. Therefore, there was no effect of carbonaceous deposits involved in the mechanism of acetylene hydrogenation in this study.

4. Conclusions

Nanocrystalline anatase titania prepared by the solvothermal method were successfully used as supports for Pd and Pd–Ag catalysts for selective hydrogenation of acetylene to ethylene. However, Pd supported on titania synthesized in toluene (higher defective sites) exhibited lower activity and selectivity for selective acetylene hydrogenation than the ones supported on titania synthesized in 1,4-butanediol (lower defective sites). Ethylene hydrogenation probably took place on the Ti^{3+} defective sites that were not in contact with palladium surface. These sites were blocked by promotion of Pd/TiO_2 with Ag metal.

Acknowledgments

The financial supports from the Thailand Japan Technology Transfer Project (TJTTP-JBIC), the Thailand Research Fund (TRF), and the Graduate School of Chulalongkorn University are gratefully acknowledged.

References

[1] M. Inoue, Y. Kondo and T. Inui, Inorg. Chem. 27 (1988) 215.
[2] M. Inoue, H. Kominami and T. Inui, J. Am. Ceram. Soc. 75 (1992) 2597.
[3] M. Inoue, H. Kominami and T. Inui, Appl. Catal. A 97 (1993) 125.
[4] H. Kominami, J.-I. Kato, S.-Y. Murakami, Y. Kera, M. Inoue T. Inui and B. Ohtani, J. Mol. Catal. A 144 (1999) 165.
[5] S. Kongwudthiti, P. Praserthdam, P.L. Silveston and M. Inoue, Ceram. Int. 29 (2003) 807.
[6] O. Mekasuwandumrong, P.L. Silveston, P. Praserthdam, M. Inoue, V. Pavarajarn and W. Tanakulrungsank, Inorg. Chem. Commun. 6 (2003) 930.
[7] W. Payakgul, O. Mekasuwandumrong, V. Pavarajarn and P. Praserthdam, Ceram. Int. (2004) in press.
[8] H. Kominami, S.-Y. Murakami, M. Kohno, Y. Kera, K. Okada and B. Ohtani, Phys. Chem. Chem. Phys. 3 (2001) 4102.
[9] B. Ohtani, K. Tennon, S.-I. Nishimoto and T. Inui, J. Photosci. 2 (1995) 7.
[10] J. Santos, J. Phillips and J.A. Dumesic, J. Catal. 81 (1983) 147.
[11] G.B. Raupp and J.A. Dumesic, J. Catal. 95 (1985) 587.
[12] M.J. Herrmann, M. Gravelle-Rumeau-Maillot and P.C. Gravelle, J. Catal. 104 (1987) 136.
[13] P. Chou and M.A. Vannice, J. Catal. 104 (1987) 1.
[14] J.H. Kang, E.W. Shin, W.J. Kim, J.D. Park and S.H. Moon, J. Catal. 208 (2002) 310.
[15] S. Ikeda, N. Sugiyama, S. Murakami, H. Kominami, Y. Kera, H. Noguchi, K. Uosaki, T. Torimoto and B. Ohtani, Phys. Chem. Chem. Phys. 5 (2003) 778.
[16] T.M. Salama, H. Hattori, H. Kita, K. Ebitani and T. Tanaka, J. Chem. Soc. Faraday Trans. 89 (1993) 2067.
[17] N. Mahata and V. Vishwanathan, J. Catal. 196 (2000) 262.
[18] S.H. Ali and J.G. Goodwin Jr., J. Catal. 176 (1998) 3.
[19] E.A. Sales, G. Bugli, A. Ensuque, M.J. Mendes and F. Bozon-Verduraz, Phys. Chem. Chem. Phys. 1 (1999) 491.
[20] D.C. Huang, K.H. Chang, W.F. Pong, P.K. Tseng, K.J. Hung and W.F. Huang, Catal. Lett. 53 (1998) 155.
[21] H. Roder, R. Schuster, H. Brune and K. Kern, Phys. Rev. Lett. 71 (1993) 2086.
[22] Y. Li, B. Xu, Y. Fan, N. Feng, A. Qiu, J. Miao, J. He, H. Yang and Y. Chen, J. Mol. Catal. A 216 (2004) 107.
[23] S. Aplund, J. Catal. 158 (1996) 267.

Jointly published by
Akadémiai Kiadó, Budapest
and Springer, Dordrecht

React.Kinet.Catal.Lett.
Vol. 86, No. 1, 141-147
(2005)

RKCL4581

DEACTIVATION OF SILICA SUPPORTED Pd CATALYSTS DURING LIQUID-PHASE HYDROGENATION

Joongjai Panpranot*, Kanda Pattamakomsan and Piyasan Praserthdam

Center of Excellence on Catalysis and Catalytic Reaction Engineering
Department of Chemical Engineering, Faculty of Engineering
Chulalongkorn University, Bangkok, 10330, Thailand

Received May 28, 2004
In revised form March 16, 2005
Accepted March 24, 2005

Abstract

Large pore MCM-41 was found to provide a better stabilization of Pd particles than amorphous SiO_2 during liquid phase hydrogenation. Pd/large pore MCM-41 exhibited higher hydrogenation activities as well as lower amount of metal loss by Pd leaching.

Keywords: Liquid-phase hydrogenation, Pd/MCM-41, Pd/SiO_2, 1-hexene hydrogenation

INTRODUCTION

Supported Pd catalysts are widely used in liquid-phase hydrogenation for many important organic transformations [1]. The nature of support affects catalyst activity, selectivity, recycling, refining, materials handling, and reproducibility. For examples, Pinna *et al.* [2] compared Pd on activated carbon, silica, and alumina in the selective hydrogenation of benzaldehyde to benzyl alcohol. Pd/Al_2O_3 was found to exhibit strong metal-support interaction while Pd/C showed the highest activity for benzaldehyde hydrogenation. Choudary *et al.* [3] reported that Pd/MCM-41 is more active in partial-hydrogenation of acetylenic compounds than Pd/Y-zeolite or Pd/K-10 clay.

* Corresponding author. Phone: +66 (02)-218-6859; Fax: +66 (02)-218-6877
E-mail: joongjai.p@eng.chula.ac.th

0133-1736/2005/US$ 20.00

However, the effects of pore size and pore structure of the same material in liquid phase hydrogenation on activity and catalyst deactivation remain unclear. In this study, the effects of silica-structure and pore size of the silica supports were investigated in terms of metal dispersion, catalytic activity in liquid-phase hydrogenation, and catalyst deactivation due to leaching and/or sintering of metal.

EXPERIMENTAL

Preparation of supported Pd catalysts

Pure silica MCM-41 with 3 nm pore diameter was prepared in the same manner as that of Cho *et al.* [4] using the gel composition of CTAB: 0.3 NH_3: 4 SiO_2: Na_2O: 200 H_2O, where CTAB denotes cetyltrimethyl ammonium bromide. The larger pore (d_{pore}= 7 nm) MCM-41 was prepared by treating the MCM-41-small pore in an emulsion containing *N,N*-dimethyldecylamine (0.625 g in 37.5 g of water for each gram of MCM-41) for 3 days at 120°C. The MCM-41 materials were calcined at 550°C (ramp rate 1-2 °C/min) in flowing nitrogen, and then in air at the same temperature for 5 h. The amorphous SiO_2-small pore with average pore diameter of 3 nm and SiO_2-large pore were obtained commercially from Grace Davison and Strem chemicals, respectively.

Supported Pd catalysts were prepared by the incipient wetness impregnation of the supports with an aqueous solution containing the desired amount of Pd nitrate dehydrate to yield a final loading of approximately 0.5 wt.% Pd. The catalysts were dried overnight at 110°C and then calcined in air at 500°C for 2 h.

Catalyst characterization

The bulk composition of palladium was determined using a Varian Spectra A800 atomic absorption spectrometer. The BET surface areas of the catalysts were determined by N_2 physisorption using a Micromeritics ASAP 2000 automated system. Each sample was degassed in the Micromeritics ASAP 2000 at 150°C for 4 h prior to N_2 physisorption. The XRD spectra of the catalysts were measured using a SIEMENS D5000 X-ray diffractometer and Cu Kα radiation with a Ni filter in the 2-10° or 20-80°2θ angular regions.

The palladium oxide particle size and distribution of palladium was observed using a JEOL-TEM 200CX transmission electron microscope operated at 100 kv. The catalyst sample was first suspended in ethanol using ultrasonic agitation for 10 min. The suspension was dropped onto a thin Formvar film supported on a copper grid and dried at room temperature before TEM

observation. Relative percentages of palladium dispersion were determined by pulsing carbon monoxide over the reduced catalyst. Approximately 0.2 g of catalyst was placed in a quartz tube, incorporated in a temperature-controlled oven and connected to a thermal conductivity detector (TCD). Prior to chemisorption, the catalyst was reduced in a flow of hydrogen (50 cm^3) at room temperature for 2 h. Then the sample was purged with helium for 1 h. Carbon monoxide was pulsed at room temperature over the reduced catalyst until the TCD signal from the pulse was constant.

Liquid-phase hydrogenation

Liquid-phase hydrogenation reactions were carried out at 25°C and 1 atm in a stainless steel Parr autoclave. Approximately 1 g of supported Pd catalyst was placed into the autoclave. The system was purged with nitrogen to remove remaining air. The supported Pd catalyst was reduced with hydrogen at room temperature for 2 h. The reaction mixture composed of 15 mL of 1-hexene and 400 ethanol was first kept in a 600 mL feed column. The reaction mixture was introduced into the reactor with nitrogen to start the reaction. The stirring rate used in this study was 1,400 rpm. It was ensured that the reaction rate does not depend on the stirring rate. The content of hydrogen consumption was monitored every five minutes by noting the change in pressure of hydrogen.

RESULTS AND DISCUSSION

Catalyst activities

Liquid-phase hydrogenation of 1-hexene was carried out as a model reaction to compare the hydrogenation activity of the MCM-41- and SiO_2-supported Pd catalysts. The kinetics study of liquid phase hydrogenation using rate of hydrogen consumption has been reported in other research investigations [3,5]. The slope of the line at the origin represents the initial rate of the reactions and the rate constant assuming zero order dependence of reaction on hydrogen [3,6]. The rate constant of the different supported Pd catalysts in liquid phase hydrogenation of 1-hexene at 25°C and the TOFs are reported in Table 1. The activity of the catalysts were found to be in the order of Pd/MCM-41-large pore > Pd/MCM-41-small pore ≈ Pd/SiO_2-large pore > Pd/SiO_2-small pore. The turnover frequencies (TOFs) were calculated based on the CO chemisorption data and are given in Table 1. Given that in all cases the support was silica, albeit in slightly different forms, it is not surprising that specific activities in the form of TOFs were so similar. Since the TOFs were similar but Pd particle

locations so disparate, it would appear that there were no pore diffusion effects on reaction rate. However, there might have been some limitations in the mass transfer of hydrogen from the gas phase to the liquid phase, given that hydrogenation is such a fast reaction on noble metals. However, we did not detect any mass transfer limitations due to pore diffusion.

Table 1

Liquid phase hydrogenation activities of various Pd catalysts[a]

Catalyst	Rate constant $x10^3$ (mol/min g cat.)	TOF (s^{-1})
Pd/SiO_2-small pore	2.45	19
Pd/SiO_2-large pore	3.40	29
Pd/MCM-41-small pore	3.41	28
Pd/MCM-41-large pore	4.75	23

[a]After 5 h batch hydrogenation of 1-hexene at 25°C and 1 atm and re-calcination at 500°C for 2 h

Catalyst deactivation due to metal sintering

The particle sizes of palladium particles before and after reaction were determined by XRD, TEM, and CO pulse chemisorption and are reported in Table 2. The fresh catalysts are referred to the catalysts after calcination in air at 500°C for 2 h. The spent catalysts were collected after one 5 h batch reaction. In order to avoid the influence of carbon deposits on the pore structure and the contrast of TEM images of the used catalysts, the spent catalysts were re-calcined in air at 500°C for 2 h before characterization to remove any carbon deposits.

Table 2

PdO and Pd^0 particle sizes before and after reaction

Catalyst	Particle size (nm)					
	XRD[a]		TEM		CO chemisorption[b]	
	Fresh	Spent	Fresh	Spent	Fresh	Spent
Pd/SiO_2-small pore	7.8	13.8	8.0	13.0	17.2	29.2
Pd/SiO_2-large pore	10.8	21.9	10.0	23.0	15.3	30.1
Pd/MCM-41-small pore	14.2	16.1	12.8	14.3	24.9	45.3
Pd/MCM-41-large pore	9.1	18.0	6.7	14.7	9.4	14.7

[a] Based on $d = (1.12/D)$ nm [9].
[b] Error of measurement = +/- 5%.

The PdO particle sizes were calculated by X-ray line broadening using the Scherrer's equation [7]. The PdO particles/clusters of the fresh catalysts were found to be ca. 8-14 nm in the order of Pd/MCM-41-small pore > Pd/SiO_2-large pore > Pd/MCM-41-large pore ≈ Pd/SiO_2-small pore. After reaction and re-calcination, it was found that the PdO particle sizes for all catalyst samples became larger, suggesting sintering of palladium metal particles [8]. Use of large pore supports resulted in the greatest amount of Pd sintering. This is probably due to the lower surface area of the supports resulting in higher probability of a metal particle to be closed to other ones and therefore the sintering probability was higher. TEM micrographs were taken in order to physically measure the size of the palladium oxide particles and/or palladium clusters. The particle sizes of PdO particles measured from TEM images before and after reaction were found to be in accordance with the results from XRD.

Pulse CO chemisorption experiments have been performed on both fresh and spent catalysts in order to determine the Pd metal particle sizes. The pulse CO chemisorption technique was based on the assumption that one carbon monoxide molecule adsorbs on one palladium site [9-12]. Average particle size

for reduced Pd^0 was calculated to be in the range of 9.4-24.9 nm before reaction and 14.7-45.3 nm after reaction. These average Pd metal particle sizes calculated based on CO chemisorption are not identical of course to the PdO particle sizes obtained by XRD and TEM.

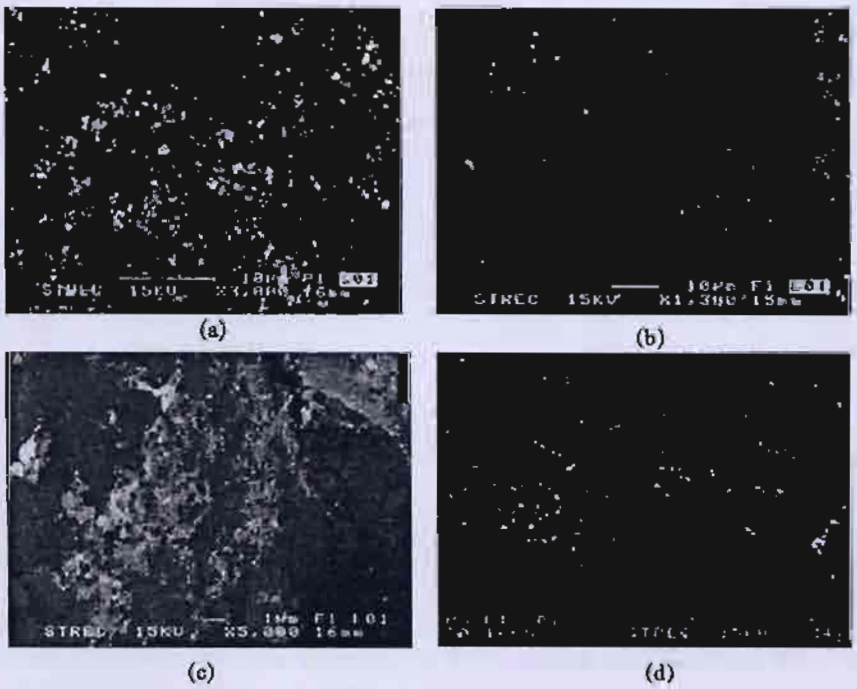

Fig. 1. SEM micrographs under back scattering mode of various silica supported Pd catalysts before and after liquid phase hydrogenation reaction (a) fresh Pd/SiO_2-small pore (b) spent Pd/SiO_2-small pore (c) fresh Pd/MCM-41-large pore (d) spent Pd/MCM-41-large pore

Catalyst deactivation due to metal leaching

SEM images in the back scattering mode shown in Fig. 1 have revealed that Pd leaching occurred during 5 h liquid phase reaction on various silica supported Pd catalysts. The actual amounts of palladium loading before and after reaction were determined by atomic adsorption spectroscopy and are given in Table 3. Before reaction, palladium loading on the catalyst samples was approximately 0.29-0.48 wt%. After one 5 h batch hydrogenation reactions of 1-hexene, palladium loading had decreased to 0.15-0.32 wt.%. The order of percentages of the amount of palladium leaching was found to be Pd/SiO_2-small

pore > Pd/SiO_2-large pore > Pd/MCM-41-small pore >> Pd/MCM-41-large pore. Pd/MCM-41-large pore showed almost no leaching of palladium into the reaction media within experimental error. The results suggest that large pore MCM-41 provided a better stabilization of small Pd particles than amorphous SiO_2 during liquid phase hydrogenation.

Table 3

Results from atomic absorption spectroscopy (AAS)

Catalyst	wt.% Pd[a]	
	Fresh	Spent
Pd/SiO_2-small pore	0.35	0.15
Pd/SiO_2-large pore	0.29	0.18
Pd/MCM-41-small pore	0.41	0.32
Pd/MCM-41-large pore	0.33	0.31

[a] Error of measurement = +/- 5%

Acknowledgement. Financial support by the Thailand Research Fund (TRF) and TJTTP-JBIC is gratefully acknowledged. The authors also thank Professor Abdel Sayari, University of Ottawa, Canada and Dr. Aticha Chaisuwan, Chulalongkorn University, Thailand for the assistance with MCM-41 preparation. We are also thankful to Prof. James G. Goodwin, Jr., Clemson University, USA, for discussion.

REFERENCES

1. P.N. Rylander: *Hydrogenation Methods*, Academic Press, New York 1985.
2. F. Pinna, F. Menegazzo, M. Signoretto, P. Canton, G. Fagherazzi, N. Pernicone: *Appl. Catal. A*, **219**, 195 (2001).
3. B.M. Choudary, M.L. Kantam, N.M. Reddy, K.K. Rao, Y. Haritha, V. Bhaskar, F. Figueras, A. Tuel: *Appl. Catal. A.* **181**, 139 (1999).
4. D.H. Cho, T.S. Chang, S.K. Ryu, Y.K. Lee: *Catal. Lett.*, **64**, 227 (2000).
5. M.K. Dalal, R.N. Ram: *Eur. Polym. J.*, **33**, 1495 (1997).
6. E.A. Sales, M. D. Mendes, F. Bozon-Verduraz: *J. Catal.*, **195**, 96 (2000).
7. H.P. Klug, L.E. Alexander: *X-Ray Diffraction Procedures for Polycrystalline Amorphous Materials*, 2nd ed., Wiley, New York 1974.
8. O. Dominguez-Quintero, S. Martinez, Y. Henriquez, L. D'Ornelas, H. Krentzien, J. Osuna: *J. Mol. Catal. A*: **197**, 185 (2003).
9. N. Mahata, V. Vishwanathan: *J. Catal.*, **196**, 262 (2000).
10. S. H. Ali, J.G. Goodwin, Jr.: *J. Catal.*, **176**, 3 (1998).
11. E.A. Sales, G. Bugli, A. Ensuque, M. J. Mendes, F. Bozon-Verduraz: *Phys. Chem. Chem. Phys.*, **1**, 491 (1999).
12. A. Sárkány, Z. Zsoldos, B. Furlong, J.W. Hightower, L. Guczi: *J. Catal.*, **141**, 566 (1993).

Journal of Porous Materials 12: 293–299, 2005

Effect of Particle Size on the Hydrothermal Stability and Catalytic Activity of Polycrystalline Beta Zeolite

JOONGJAI PANPRANOT*, USNEE TOOPHORM AND PIYASAN PRASERTHDAM
Center of Excellence on Catalysis and Catalytic Reaction Engineering, Department of Chemical Engineering, Chulalongkorn University, Bangkok 10330, Thailand
Joongjai.P@eng.chula.ac.th

Received January 5, 2005; Revised March 21, 2005

Abstract. The effect of particle size in the range of 0.2–0.9 μm on the hydrothermal stability of polycrystalline beta zeolites was investigated in terms of changes in BET surface areas, percent crystallinity, and framework aluminum atoms. It was found that the hydrothermal stability of beta zeolite increased with increasing particle size while the catalytic activities decreased. However, the XRD results have revealed that percent crystallinity of the hydrothermally treated beta zeolite remained relatively high (>95%) although dealumination occurred in most cases. This high stability is due probably to small amount of Al atoms present in the unit cell of this zeolite.

Keywords: beta zeolite, particle size effect, hydrothermal stability, methanol conversion

1. Introduction

Beta zeolite first synthesized by the Mobil Oil researchers [1] possesses a three dimensional large pore system of a 12-membered ring with two different types of channels, which are 0.7 and 0.5 nm wide. Beta zeolite has been studied in many catalytic reactions such as alkane isomerization [2], aromatic alkylation [3], aromatic acylation [4], aromatic nitration [5], aliphatic alkylation [6], and indole synthesis [7]. The commercial beta zeolite is generally synthesized with particle size less than 1 μm. Although smaller particles of zeolites were often found to be more active due to less diffusion constraint of the reactants and products, they were less stable than larger ones. Praserthdam et al. [8] have investigated the effect of crystal size on the durability of Co/HZSM-5 in selective reduction of NO. The smaller crystal size Co/HZSM-5 showed the greater durability. The role of particle size in the catalytic activity of beta zeolite has been reported by a number of groups [2, 9–11]. Bonetto et al. [9] studied the catalytic performances of beta zeolite with three different particle sizes (0.17, 0.40, and 0.70 μm) in gasoil cracking. The beta zeolite with the particle size of 0.40 μm was found to produce the highest liquefied petroleum gas and iso-butane yield. Arribus and Martinez [2] showed that the catalytic performance of Pt/Beta zeolite catalysts in simultaneous isomerization of *n*-heptane and saturation of benzene could be improved by decreasing the zeolite crystal size.

Thus, in previous studies, the effects of crystal or particle size on the catalytic performance of zeolites have been studied and compared. However, the effect of particle size on the structural stability under hydrothermal conditions of polycrystalline beta zeolite has not been studied to a great extent. In this study, a correlation between particle size and hydrothermal stability of polycrystalline beta zeolites was investigated by means of various characterization techniques such as X-ray diffraction, N_2 physisorption, nuclear magnetic resonance (NMR), and scanning electron microscopy. The catalytic activities of beta zeolites were also tested in methanol conversion.

*To whom correspondence should be addressed.

2. Experimental

2.1. *Synthesis of H-Beta Zeolite*

The hydrogen form of beta zeolite with different particle sizes was prepared as reported elsewhere [12] using hydrothermal method and the following gel composition: K_2O:2Na_2O:12.5TEAOH: 1/2Al_2O_3:30SiO_2:700H_2O, where TEAOH denotes tetraethylammonium hydroxide. The mixture of synthesis reagents was stirred under vigorous magnetic stirring before transferring into a stainless steel autoclave. Then it was heated from room temperature to 135°C in 1 h under a pressure of nitrogen at 3 kg/cm^2 and maintained at this condition for 40 h. The obtained solid material was filtered, washed with deionized water until pH = 9, and dried overnight in an oven at 110°C. The sample was then calcined in air at 540°C (8.5°C/min) for 3.5 h. The hydrogen form of beta zeolite was obtained by first exchanging Na^+ with NH^{4+} using an aqueous solution of NH_4NO_3 and subsequently decomposing the NH^{4+} by calcination in air at 500°C for 2 h.

2.2. *Hydrothermal Treatment*

Hydrothermal treatment of the catalysts was performed in a home-made system. Approximately 0.5 g of catalyst sample was placed in the reactor and was first heated in a He flow to 600°C using a ramp rate of 10°C/min then from 600–800°C using a ramp rate of 1.7 °C/min. It was kept at this final temperature for 30 min under 10 mol% water vapor. Finally, it was cooled down to room temperature in a He stream.

2.3. *Catalyst Characterization*

Average particle size and particle size distribution of the catalysts before and after hydrothermal treatment were determined visually from SEM micrographs obtained from a JEOL JSM-35 CF model scanning electron microscope. The crystallinity of the zeolite was determined using X-ray diffractometer (SIEMENS D5000) with monochromatized Cu K_α radiation (10 kV, 20 mA). Percent crystallinity was calculated based on the area of the main peak compared with that of fresh beta zeolite as a reference. Specific surface areas of the zeolite were calculated using a BET single point method from the measured amount of N_2 uptake at liquid nitrogen boiling point temperature using a GOW-MAC gas chromatograph. Quantities of Si and Al in the sample were determined using a FISONS ARL8410 XRF analyzer. The chemical state of Al was measured by ^{27}Al MAS-NMR using a BRUKER DPX-300 NMR spectrometer operated at 78.2 MHz at the magic angle. The relative area of tetrahedral ^{27}Al was calculated from the area of tetrahedral aluminum per summation area of tetrahedral and octahedral aluminum.

2.4. *Reaction Study*

Methanol conversion was performed in a down-flow differential fixed-bed quartz tubular reactor. A GHSV of ca. 4,000 h^{-1} and a 20 mol% methanol were used. Approximately 0.2 g catalyst was held in the middle of the reactor using quartz wool. It was first heated in a 50 cc/min N_2 flow to 450°C, using a ramp rate of 10°C/min and held at this temperature for 30 min prior to reaction. The reaction was initiated by allowing the N_2 flow to pass through the reactants inside the saturator in the water bath. After the start-up for 1 h, samples were taken and analyzed by a GC (Shimadzu GU-14A). The catalytic activity was evaluated based on the conversion of methanol to hydrocarbons.

3. Results and Discussion

Scanning electron micrographs of beta zeolite samples with various crystallite sizes are shown in Fig. 1. Typically a spherical shape was formed for all crystallite sizes of beta zeolites. The average crystal sizes of the samples were measured from scanning electron micrographs by averaging the diameters of a hundred primary particles. The effect of particle size on the

Table 1. The effect of particle size on the percent decrease in specific surface areas of beta zeolite after hydrothermal treatment.[a]

Particle size (μm)	Specific surface area (m^2/g)		% decrease of S.A.
	Fresh	Treated	
0.2	612	490	19.9
0.3	579	481	16.9
0.4	500	459	8.2
0.5	464	446	3.9
0.7	382	364	4.7
0.9	374	355	5.1

[a]Hydrothermal treatment conditions were 800°C, 10 mol% water vapor, and 30 min.

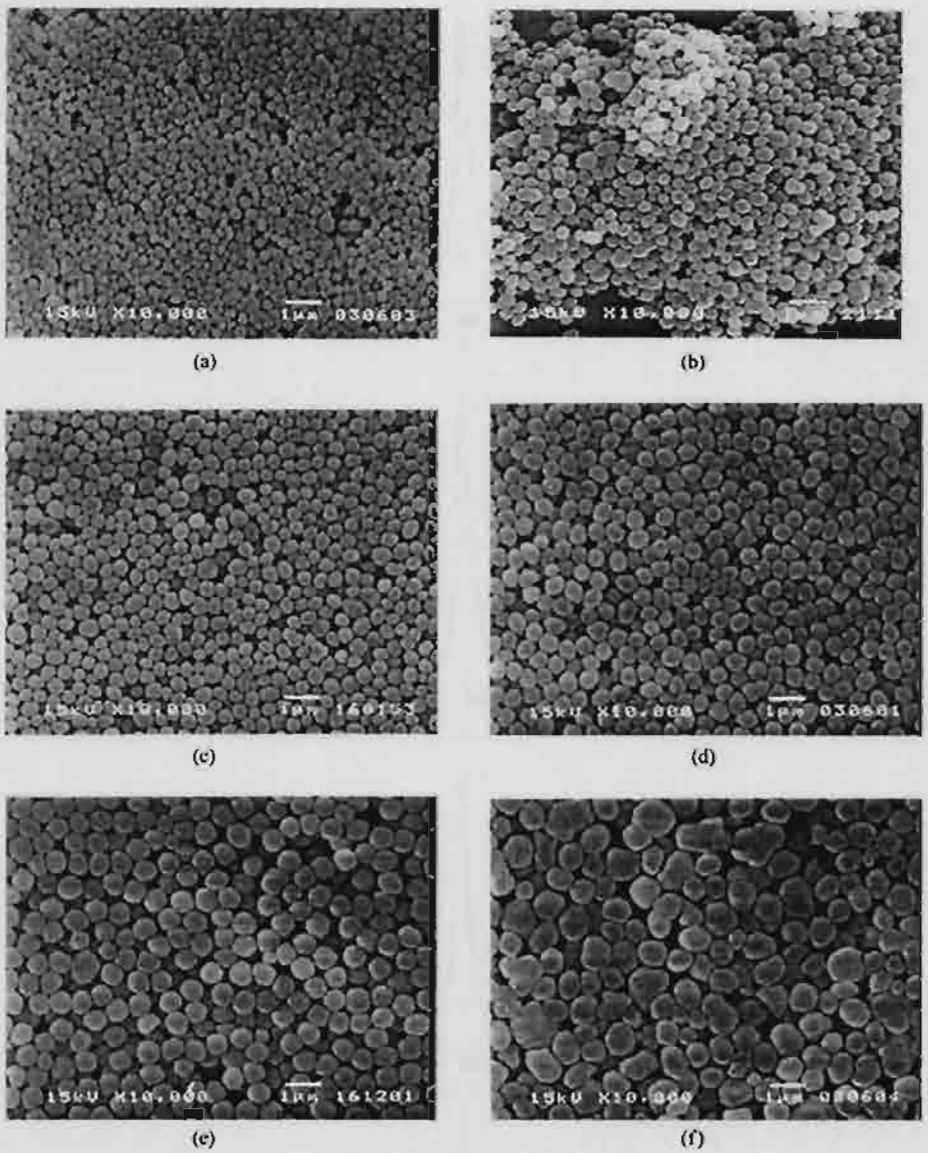

Figure 1. SEM micrographs of beta zeolites with various particle sizes (a) 0.2 μm, (b) 0.3 μm, (c) 0.4 μm, (d) 0.5 μm, (e) 0.7 μm and (f) 0.9 μm.

percent decrease of surface areas of beta zeolites after hydrothermal treatment at 800°C with 10 mol% water vapor for 30 min is shown in Table 1. It was found that the surface areas of beta zeolite samples with the crystallite sizes in the range of 0.2–0.4 μm decreased significantly after hydrothermal treatment with the particle size of 0.2 μm showed the highest loss of surface area (ca. 20%). The beta zeolites with larger particle sizes ranging from 0.5–0.9 μm showed only 4–5% decrease in surface areas. A loss of surface area upon hydrothermal treatment suggests a partial collapse of zeolite framework [10–14].

The environment of the aluminum atoms in the zeolite samples was studied using ^{27}Al MAS NMR spectroscopy. Figure 2 presents the ^{27}Al MAS NMR spectra of H-beta zeolite with particle sizes of 0.3 and 0.9 μm before and after hydrothermal treatment. The tetrahedral Al presented in the zeolite framework ($Al(OSi)_4$)

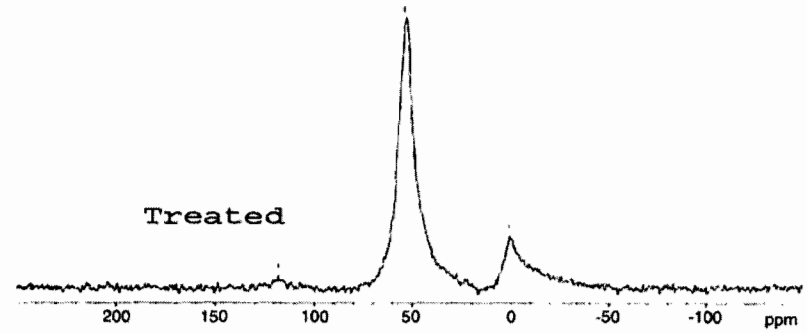

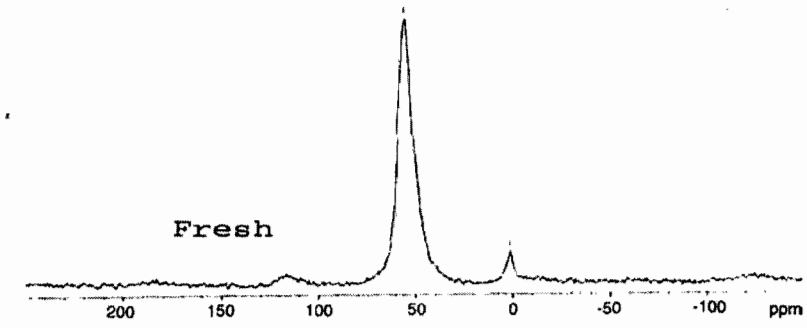

(a)

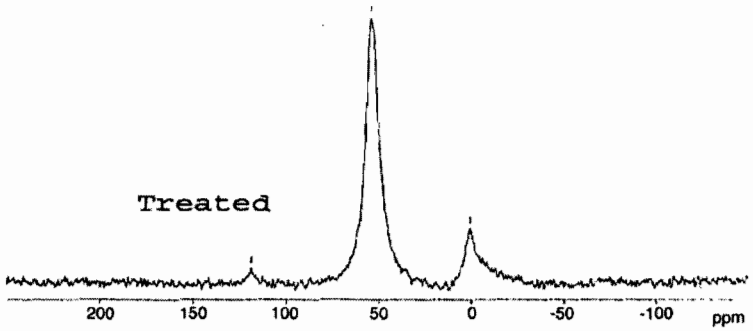

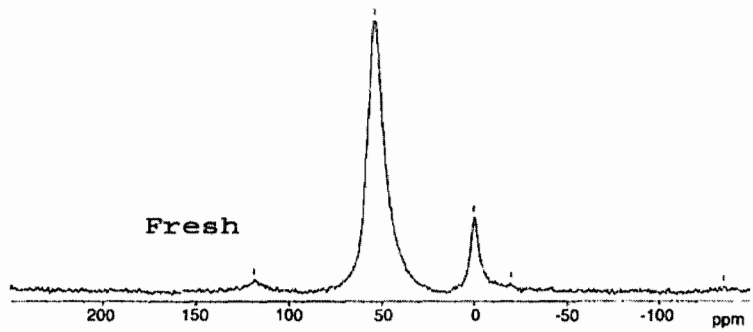

(b)

ure 2. (a) NMR spectra of beta zeolites with particle size of 0.3 μm before and after hydrothermal treatment. (b) NMR spectra of beta. olites with particle size of 0.9 μm before and after hydrothermal treatment.

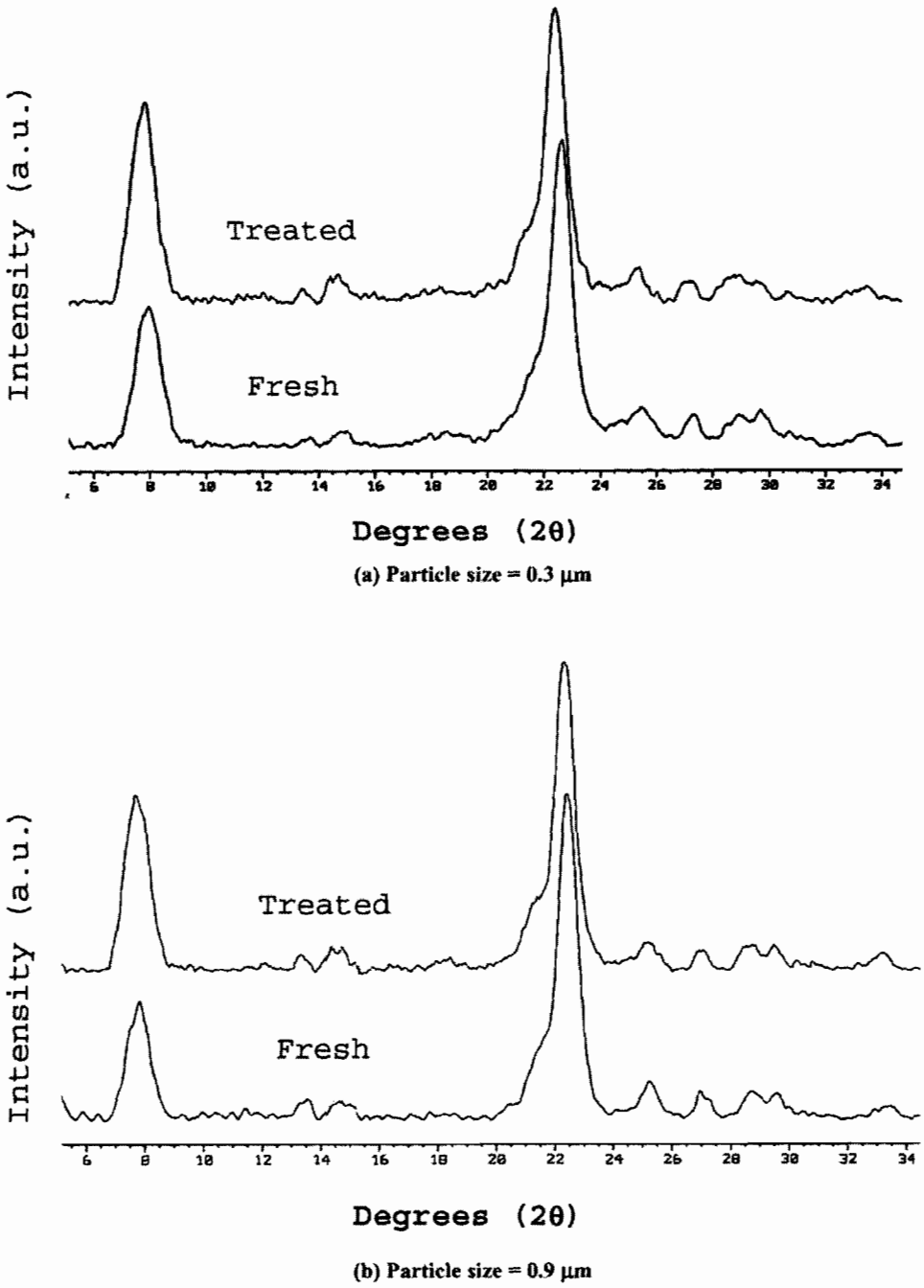

Figure 3. XRD patterns of beta zeolites with different particle sizes.

is shown by NMR signal at ca. 52 ppm while extra-framework aluminum (EFAl) species which are usually octahedrally coordinated is shown at a chemical shift of ca. 0 ppm [13, 14]. A strong peak of tetrahedrally coordinated framework Al and a very weak signal of octahedral EFAl were found in all samples. The EFAl species in the fresh samples were probably formed during the calcinations in the preparation

Table 2. The effect of particle size on the percent decrease of tetrahedral ^{27}Al and % crystallinity after hydrothermal treatment.[a]

Particle size (μm)	The relative areas of tetrahedral ^{27}Al (%)		% decrease of tetrahedral ^{27}Al	% crystallinity after hydrothermal treatment
	Fresh	Treated		
0.2	94	77	18.1	95
0.3	95	78	17.9	95
0.4	93	79	15.1	96
0.5	88	78	11.4	97
0.7	89	81	9.0	96
0.9	94	78	17.0	95

[a]Hydrothermal treatment conditions were 800°C, 10 mol% water vapor, and 30 min.

procedure to transform as-synthesized to H-form beta zeolites [15]. After hydrothermal treatment, a decrease in tetrahedral aluminum and an increase in octahedral aluminum were observed for all particle sizes of beta zeolites used in this study, suggesting that dealumination occurred upon hydrothermal treatment. The relative areas of tetrahedral ^{27}Al were calculated from the area of tetrahedral aluminum per summation area of tetrahedral and octahedral aluminum and are given in Table 2. The beta zeolite with particle size of 0.7 μm was found to exhibit the lowest extent of dealumination. It should be noted that upon hydrothermal treatment of beta zeolite besides dealumination, formation of mesoporosity has also been observed [16–18].

The XRD patterns of beta zeolite before and afte hydrothermal treatment for different crystallite size are shown in Fig. 3. The two characteristic peaks o H-beta zeolite at 2θ 7.8° and 22.4° were detected. Th percent crystallinity of the samples was calculated b comparing the peak intensities of the treated sample with the fresh samples. The 22.4° peak was chosen fo comparison since it was found to be a major character istic peak of H-beta zeolite [19–21]. It was found tha the relative % crystallinity of the samples remaine as high as 95–97% after hydrothermal treatment. Du probably to the presence of only 3–4 Al atoms in th unit cell, the crystallinity of the zeolite does not signif icantly change although all the Al atoms are remove from the framework [11, 12, 22]. Similar result was als

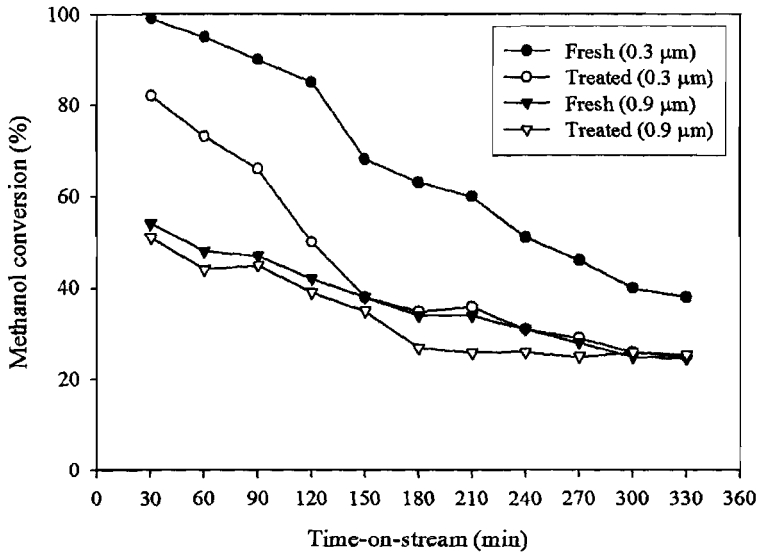

Figure 4. Methanol conversion over fresh and hydrothermally treated beta zeolite with different particle sizes.

found for dealumination of ZSM-5 zeolite as reported by Traintafillidis et al. [23].

Samples of fresh and hydrothermally treated beta zeolites with different particle sizes have been tested for catalytic activities in methanol conversion. The results of methanol conversions as a function of time-on-stream are shown in Fig. 4. It was found that smaller particle size of beta zeolites exhibited higher activities in methanol conversion than the larger ones. And for a given particle size, the activities of untreated catalysts were higher than the hydrothermal treated ones in all ranges of time-on-stream. The activities of the beta zeolite with smaller particle size, however, decreased significantly with time-on-stream while for larger particle size the initial activities and after 330 min on stream were not significantly different. The results were found to be in agreement with the well-established trends in the literature that smaller particle zeolites were more active than those of larger particle ones. However, it should be emphasized that our results support the need for a balance between hydrothermal stability and high catalytic activity. Thus, an appropriate particle size of beta zeolite must be carefully chosen, especially when the reaction is carried out under severe hydrothermal conditions.

4. Conclusions

The hydrothermal stability and catalytic activity of beta zeolite were found to be dependent on the particle size. While the hydrothermal stability increased with increasing particle size, the catalytic activity in methanol conversion changed in the opposite direction. The hydrothermal treatment caused dealumination of the zeolite framework, decreased BET surface areas, and lowered catalytic activities. However, hydrothermal treatment did not alter the relative crystallinity of beta zeolite due probably to the small amount of Al atoms presented in the unit cell.

Acknowledgment

The financial supports from the Thailand Research Fund (TRF) and TJTTP-JBIC are gratefully acknowledged.

References

1. R.L. Wadlinger, G.T. Kerr, and E.J. Rosinski, US Patent N(3,308,069, Mobil oil Corp. (1967).
2. M.A. Arribas and A. Martinez, Catal. Today **65**, 117 (2001).
3. G. Bellusi, G. Pazzuconi, C. Perego, G. Girotti, and G. Terzon J. Catal. **157**, 227 (1995).
4. A.J. Hoefinagel and H. van Bekkum, Appl. Catal. A **97**, 8 (1993).
5. K. Smith, A. Musson, and G.A. DeBoos, J. Chem. Soc. Chen Commun. **469** (1996).
6. K.P. de Jong, C.M.A.M. Mesters, D.G.R. Peferoen, P.T.M van Brugge, and C. de Groot, Chem. Eng. Sci. **51**, 205 (1996).
7. M.S. Rigutto, H.J.A. de Vries, S.R. Magill, A.J. Hoefi nagel, and H. van Bekkum, Stud. Surf. Sci. Catal. **78**, 66 (1993).
8. P. Praserthdam, N. Mongkolsiri, and P. Kanchanawanichkun Catal. Commun. **3**, 191 (2002).
9. L. Bonetto, M.A. Camblor, and A. Corma, Appl. Catal. A **82** 37 (1992).
10. F. Vaudry, F. Di renzo, F. Fajula, and P. Schulz, J. Chem, Soc. Faraday Trans. **94**, 617 (1998).
11. P. Sharma, Y. Igushi, Y. Sekine, E. Kikuchi, and M. Matsukata Stud. Surf. Sci. Catal. **145**, 219 (2003).
12. J. Perez-Pariente, J.A. Martens, and P.A. Jacobs, Zeolites **8**, 4((1988).
13. J. Sanz, V. Fornés, and A. Corma, J. Chem, Soc., Faraday Trans **84**, 3113 (1988).
14. J.P. Jilson, G.C. Edwards, A.W. Peters, K. Rajagopalan, R.F Wormsbecher, T.G. Roberie, and M.P. Shatlock, J. Chem. Soc. Chem. Commun. **91** (1987).
15. B.B. Ramesh and P.A. Clearfield, J. Phys. Chem. **96**, 672((1992).
16. S. Bernasconi, J.A. van Bokhoven, F. Krumeich, G.D. Pirngru ber, and R. Prins, Microporous and Mesoporous Mater. **66**, 2 (2003).
17. M.V. Landau, D. Taylor, O. Regev, M.L. Kaliya, M. Herskowitz V. Valtchev, and S. Mintova, Chem. Mater. **11**, 203((1999).
18. M.A. Camblor, A. Corma, A. Mifsud, J. Perez-Pariente S. Valencia, Stud. Surf. Sci. Catal. **105A**, 341 (1997).
19. A.M. Camiloti, S.L. Jahn, N.D. Velasco, L.F. Moura, and D Cardoso, Appl. Catal. A **182**, 107 (1999).
20. P.J. Kunkeler, B.J. Zurdeeg, J.C. van der Waal, J.A. vai Bokhoven, D.C. Koningsberge, and H. van Bekkun, J. Catal **180**, 234 (1998).
21. R. Szoztak, *Molecular Sieve Principles of Synthesis an Identification* (van Nostrand Reingold, New York, 1989) pp. 1–50.
22. C.T. Costa, G.V. Athanasios, L. Nalbandian, and P.E. Nicholas Microporous and Mesoporous Mater. **47**, 369 (2001).
23. C.S. Triantafillidis, A.G. Vlessidis, and N.P. Evmiridis, Ind. Eng Chem. Res. **39**, 307 (2000).

Available online at www.sciencedirect.com
SCIENCE DIRECT
Materials Chemistry and Physics 94 (2005) 207–212
MATERIALS CHEMISTRY AND PHYSICS
www.elsevier.com/locate/matchemphys

Glycothermal synthesis of nanocrystalline zirconia and their applications as cobalt catalyst supports

Joongjai Panpranot*, Nuttakarn Taochaiyaphum, Piyasan Praserthdam

Center of Excellence on Catalysis and Catalytic Reaction Engineering, Department of Chemical Engineering, Chulalongkorn University, Bangkok 10330, Thailand

Received 8 December 2004; received in revised form 3 March 2005; accepted 19 April 2005

Abstract

Nanocrystalline zirconia have been prepared by the glycothermal method with two different glycols (1,4-butanediol and 1,5-pentanediol) and employed as the support for cobalt catalysts. Commercial zirconia supported cobalt catalyst was also prepared and used as a reference material. The glycothermal-derived zirconia possesses large surface areas with crystallite sizes of 3–4 nm. The catalytic activities for CO hydrogenation of the glycothermal-derived zirconia supported cobalt catalysts were found to be much higher than that of the commercial zirconia supported one. However, the cobalt catalysts supported on zirconia prepared in 1,4-butanediol with lower amount of Zr content in the starting solution exhibited higher activities than the ones supported on zirconia prepared in 1,5-pentanediol. The results suggest that the different crystallization mechanism occurred in the two glycols may affect the amount of crystal defects produced in the corresponding zirconia. As shown by TPR profiles, lower metal-support interaction was observed for the catalysts supported on the zirconia formed via solid-state reaction in 1,4-butanediol (more defects). Consequently, higher active surface cobalt was available for H_2 chemisorption and CO hydrogenation reaction.

Keywords: A. Nanocrystalline zirconia; B. Glycothermal method; Zirconia supported cobalt

1. Introduction

Zirconia powder has been effectively used in different areas of chemistry such as in ceramics and catalysis. It has been found that zirconia has high catalytic activities for isomerization of olefins [1] and epoxides [2]. Commercially available zirconia, however, usually possesses low BET surface area (<50 $m^2\,g^{-1}$) thus may have limited their uses as catalyst supports where a high dispersion of metal is required in order to have high catalytic activity. Recently, synthesis of a high surface area nanocrystalline zirconia has been developed by Inoue et al. [3,4] and is so-called the glycothermal or solvothermal method depending on the solvent used. By thermal decomposition of zirconium alkoxide in organic solvents, large surface area zirconia can be obtained directly without bothersome procedures such as purification of the reactants or handling in an inert atmosphere. Nanocrystals were formed when the starting materials were completely dissolved into the solvent. However, apparently polycrystalline outlines can be observed due to rapid crystal growth [5]. Processing variables such as pH, concentration, temperature, reaction medium, and crystallization time have influences on the crystal structure of zirconia [6–9].

In this study, nanocrystalline zirconia were prepared by the glycothermal method in two different glycols and used as supports for cobalt catalysts. The influences of the glycol source and the Zr concentration in the starting materials on the physicochemical properties of the zirconia were investigated by means of N_2 physisorption, XRD, and SEM. The corresponding glycothermal-derived zirconia supported cobalt catalysts were further characterized by H_2 chemisorption, temperature programmed reduction, and were tested for catalytic activities in CO hydrogenation reaction.

* Corresponding author. Tel.: +66 2 218 6859; fax: +66 2 218 6877.
E-mail address: joongjai.p@eng.chula.ac.th (J. Panpranot).

0254-0584/$ – see front matter © 2005 Elsevier B.V. All rights reserved.
doi:10.1016/j.matchemphys.2005.04.035

2. Experimental

2.1. Preparation of zirconia

Nanocrystalline zirconia was prepared by the glycothermal method according to the procedure described in Ref. [9]. Approximately 15 g of zirconium tetra *n*-propoxide, $Zr(OC_3H_7)_4$ (ZNP) with 20.5% Zr from Strem Chemicals or ZNP with 29.5% Zr from Mitsuwa Pure Chemicals was added to 100 ml of a glycol (1,4-butanediol (Aldrich) or 1,5-butanediol (Merck). This mixture was placed in a 300 ml-autoclave. After the atmosphere inside the autoclave was replaced with nitrogen, the mixture was heated to 300 °C at a heating rate of 2.5 °C min^{-1} and was kept at that temperature for 2 h. After cooling to room temperature, the resulting powders were collected after repeated washing with methanol. The products were then air-dried and were used without further calcinations. For comparison purposes, commercial zirconium dioxide was obtained from Aldrich.

2.2. Catalyst preparation

The zirconia supported cobalt catalysts were prepared by incipient wetness impregnation method using Co(II) nitrate hexahydrate (Aldrich). The catalysts were dried overnight at 110 °C and then calcined in air at 300 °C for 2 h. The final cobalt loading of the calcined catalysts were determined using atomic absorption spectroscopy (Varian Spectra A800) to be ca. 8 wt%.

2.3. Catalyst nomenclature

The different glycothermal-derived zirconia are designated as ZrO_2–BG-20, ZrO_2–BG-30, ZrO_2–PeG-20, and ZrO_2–PeG-30 in which BG and PeG refer to the glycol used (BG = 1,4-butanediol, PeG = 1,5-pentanediol) and the number 20 and 30 refer to the concentration of Zr in the ZNP solution used. Commercial zirconia was designated as ZrO_2-com. Cobalt catalysts supported on different zirconia are designated as Co/ZrO_2–BG-20 for Co supported on ZrO_2–BG-20 and so on.

2.4. Catalyst characterization

The BET surface areas were determined by N_2 physisorption using a Quantachrome Nova 1000 automated system. Each sample was degassed in the system at 150 °C for 2 h prior to N_2 physisorption. The XRD spectra of the sample powders were measured using a SIEMENS D5000 X-ray diffractometer using Cu Kα radiation with a Ni filter in the 10–80° 2θ angular regions. The particle morphology was obtained using a JEOL JSM-35CF scanning electron microscope (SEM) operated at 20 kV. H_2 chemisorption was carried out following the procedure described by Reuel and Bartholomew [10] using a Micromeritics Pulse Chemisorb 2700 system. Prior to chemisorption, the catalysts were reduced at 350 °C for 10 h after ramping at a rate of 1 °C min^{-1}. Static H_2 chemisorption was performed at 100 °C. The TPR profiles of supported cobalt catalysts were obtained by temperature programmed reduction using an in-house system and a temperature ramp of 5 °C min^{-1} from 30 to 500 °C in a flow of 5% H_2 in argon. Approximately 0.20 g of a calcined catalyst was placed in a quartz tube in a temperature-controlled oven and connected to a thermal conductivity detector (TCD). The H_2 consumption was measured by analyzing the effluent gas with a thermal conductivity detector.

2.5. CO hydrogenation reaction

CO hydrogenation was carried out at 220 °C and 1 atm total pressure in a fixed-bed stainless steel reactor under differential conversion conditions. A flow rate of H_2/CO/Ar = 20/2/8 cm^3 min^{-1} was used. Typically, 0.2 g of the catalyst samples was reduced in situ in flowing H2 (50 cm^3 min^{-1}) at 350 °C for 10 h prior to reaction. The product samples were taken at 1 h intervals and analyzed by gas chromatography. Steady state was reached after 6 h time-on-stream in all cases. The percentages of CO conversion and reaction rates were defined as

$$\%\text{CO conversion} = \frac{\text{mole of CO in feed} - \text{mole of CO in products}}{\text{mole of CO in feed}} \times 100$$

$$\text{reaction rate (g CH}_2\text{ g cat.}^{-1}\text{ h}^{-1}) = \frac{\%\text{CO conversion} \times \text{flowrate of CO in feed(cm}^3\text{ min}^{-1}) \times 60\text{ min h}^{-1} \times \text{mol.wt. of CH}_2\text{(g mol}^{-1})}{\text{catalyst weight(g)} \times 22400\text{ cm}^3\text{ mol}^{-1}}$$

3. Results and discussion

The X-ray diffraction patterns of the zirconia powders prepared by the glycothermal method in two different glycols with various Zr contents in the ZNP solutions and the commercial zirconia are shown in Fig. 1. All the glycothermal-derived zirconia samples exhibited tetragonal crystalline zirconia phase. No other crystal structures were observed. The crystal structure of the commercial zirconia as observed from XRD shows a mixture of tetragonal and monoclinic phases, typical for a commercial one. The average crystallite sizes calculated from the XRD line broadening using the Scherrer's equation [11] and the BET surface areas of the zirconia are reported in Table 1. The average crystallite sizes of the glycothermal-derived zirconia were approximately 3–4 nm while that of the commercial zirconia were found to be ca. 10.5 nm. The BET surface areas of the glycothermal-derived zirconia were found to be much higher (195–220 m^2 g^{-1}) than that of a commercial

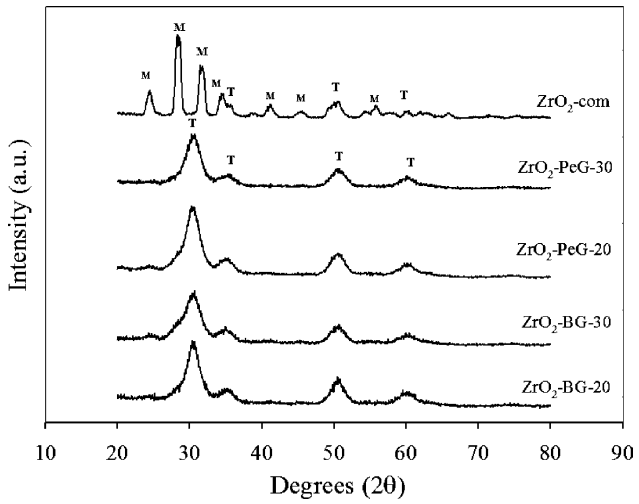

Fig. 1. X-ray diffraction patterns of the zirconia (T = tetragonal, M = monoclinic).

zirconia (50 $m^2\ g^{-1}$). Within experimental error, there was no significant difference in BET surface areas and the crystallite sizes of the zirconia prepared in different glycols or prepared with different amounts of Zr content in the ZNP solution.

Typical SEM micrographs of zirconia samples prepared in 1,4-butanediol and 1,5-pentanediol with different Zr contents are shown in Fig. 2. It was reported that when the starting material were completely dissolved into the glycol, nanocrystals were formed [5]. Each particle was, therefore, a single crystal grown from a nucleus. It was found that the samples prepared in 1,4-butanediol have a spherical shape and a dense mass while in 1,5-pentanediol the samples did not form separate spherical particles. The secondary particles which appeared as separate spherical particles when prepared in 1,4-butanediol seem to be formed by aggregation of primary particles. The results were found to be in agreement with the work previously reported by our group on the effect of solvent on the preparation of zirconia by glycothermal method [9]. It has been proposed by Praserthdam et al. [9] that the mechanisms during crystallization of zirconia in the two glycols were completely different. While the synthesis in 1,5-pentanediol, a homogeneous solution (i.e., glycoxide) was formed after the mixture was heated to 250 °C and cooled down, the synthesis in 1,4-butanediol yielded a solid precipitate. The authors suggested that crystal growth of zirconia in 1,5-pentanediol proceeded by precipication and crystallization of the glycoxide while zirconia particles crystallized from solid-state transformation in 1,4-butanediol.

Table 1
The characteristics of the zirconia samples

Sample	Average crystallite size[a] (nm)	Crystal structure[b]	BET surface area[c] ($m^2\ g^{-1}$)
ZrO_2–BG-20	4.0	T	206
ZrO_2–BG-30	3.0	T	195
ZrO_2–PeG-20	3.7	T	220
ZrO_2–PeG-30	3.6	T	207
ZrO_2-com	10.5	T, M	50

[a] Based on XRD line broadening.
[b] T = tetragonal, M = monoclinic.
[c] Error of measurement = ±10%.

The characteristics and catalytic activities for CO hydrogenation of various zirconia supported cobalt catalysts are shown in Table 2. In this study, cobalt loading on the catalyst samples was approximately 8 wt% in order to make it close to that required for a commercial cobalt catalyst used in the Fischer–Tropsch synthesis. The BET surface areas of the zirconia supported cobalt catalysts were slightly less than that of the original zirconia supports suggesting that cobalt was deposited in some of the pores of zirconia. It would appear that the particle size and shape of the catalyst particles were not affected by impregnation of cobalt since no physical changes were observed. The X-ray diffraction patterns of the zirconia-supported cobalt catalysts are shown in Fig. 3. The XRD diffraction peaks for cobalt oxide (Co_3O_4) at ca. 31.3°, 36.8°, 45.1°, 59.4°, and 65.4° 2θ were not clearly seen for all the catalyst samples except for the Co/ZrO_2-com where a small peak at ca. 36.8° 2θ was apparent. The results suggest that the crystallite sizes of cobalt oxide on the glycothermal-derived zirconia were probably smaller than the lower limit of XRD detectability (3–5 nm). It is also possible that on glycothermal-derived zirconia, cobalt did not form Co_3O_4 crystallites but may have formed an amorphous cobalt oxide [12]. The non-appearance of the XRD characteristic peaks for cobalt oxides was similar to the results obtained from cobalt supported on other metal oxides prepared by sol–gel technique that usually possesses very small cobalt particles [13–18].

The relative amounts of active cobalt metals on the catalyst samples were calculated from H_2 chemisorption experiments at 100 °C according to Reuel and Bartholomew [10]. It is known that only surface cobalt metal atoms are active for CO hydrogenation not its oxide or carbide [19]. It was found that our glycothermal-derived zirconia supported cobalt catalysts exhibited much higher H_2 chemisorption and CO hydrogenation activities than the commercial zirconia supported one with Co/ZrO_2–BG-20 exhibited the highest amount of H_2 chemisorption and CO hydrogenation activity. It should be noted that differences in the amount of H_2 chemisorption and the catalytic activities among the glycothermal-derived zirconia supported catalysts were not due to difference in the BET surfaces areas or the crystallite sizes of zirconia because within experimental error the BET surface areas for all the glycothermal-derived zirconia supported cobalt catalysts and the crystal sizes of zirconia were quite similar. However, the crystallization mechanism in the two glycols probably yielded the final zirconia particles with different amount of crystal defects. Since crystal defects were frequently created especially when crystal growth proceeded rapidly, zirconia prepared in 1,4-butanediol which was found to form via solid-state reaction would contain more crystal defects compared to the ones prepared in 1,5-pentanediol which crystallized via precipitation of alkoxide solution. These defects in the zirco-

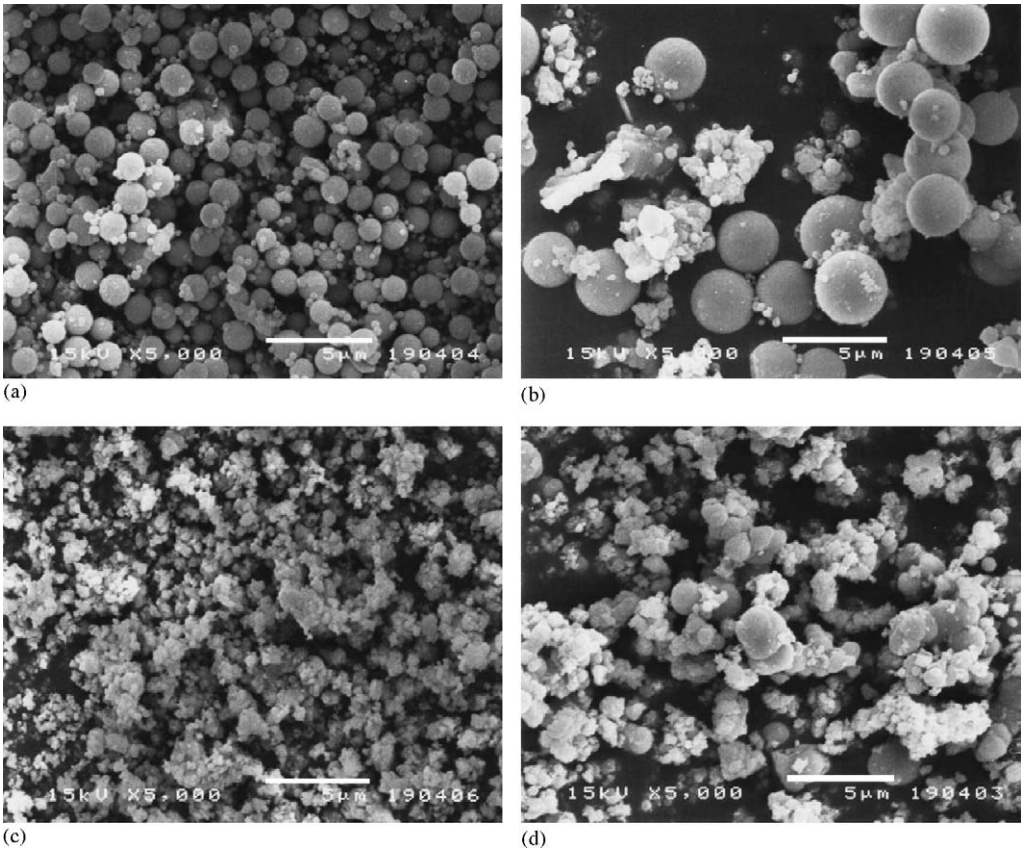

Fig. 2. SEM micrographs of (a) ZrO_2–BG-20 (b) ZrO_2–BG-30 (c) ZrO_2–PeG-20 and (d) ZrO_2–PeG-30.

nia particles may play a role in cobalt-support interaction in supported cobalt catalysts.

Fig. 4 shows the temperature program reduction (TPR) profiles of various zirconia supported cobalt catalysts. TPR is a powerful tool to study the reduction behavior of the catalysts. Reduction of cobalt in the oxide form, Co_3O_4 or Co_2O_3, to Co^0 involves a two-step reduction: first reduction of Co_3O_4 to CoO and then the subsequent reduction of CoO to Co^0 [20,21]. The two reduction steps may not always be observed as separate peaks in TPR profile, as seen in Fig. 4 for the reduction of bulk Co_3O_4 powder [22]. However, a separation of the two reduction steps has often been found for supported cobalt catalysts due to interactions between cobalt and support materials [23,24]. A wide range of variables such as metal particle size and metal-support interaction have an influence on the reduction behavior of cobalt catalysts resulting in the observation of different locations of the TPR peaks. Since the catalysts were pre-calcined at 300 °C, the nitrate precursor has been completely thermally decomposed below 300 °C [25]. Therefore, the hydrogen consumption observed during TPR study cannot be ascribed to residual nitrates. The TPR profiles of the glycothermal-derived zirconia supported cobalt catalysts were different from that of the commercial zirconia supported one in which the reduction

Table 2
The characteristics and catalytic activities of the zirconia supported Co catalysts for CO hydrogenation reaction

Catalyst	BET S.A.[a] ($m^2\ g^{-1}$)	H_2 chemisorption[b] ($\times 10^{18}$ mol g cat^{-1})	Reaction rate[c] (g CH_2 g cat^{-1} h^{-1})	Product selectivity (%)		
				CH_4	C_2–C_3	C_{4+}
Co/ZrO_2–BG-20	170	12.9	14.5	29.5	11.4	59.1
Co/ZrO_2–BG-30	160	6.7	12.0	53.6	11.7	34.8
Co/ZrO_2–PeG-20	173	5.9	7.7	70.7	4.2	25.1
Co/ZrO_2–PeG-30	180	5.8	6.4	73.4	7.5	19.1
Co/ZrO_2-com	46	3.1	3.8	77.8	8.6	13.5

[a] Error of measurement = ±10%.
[b] Error of Measurement = ±5%.
[c] Reaction conditions were 220 °C, 1 atm, and H_2/CO ratio = 10.

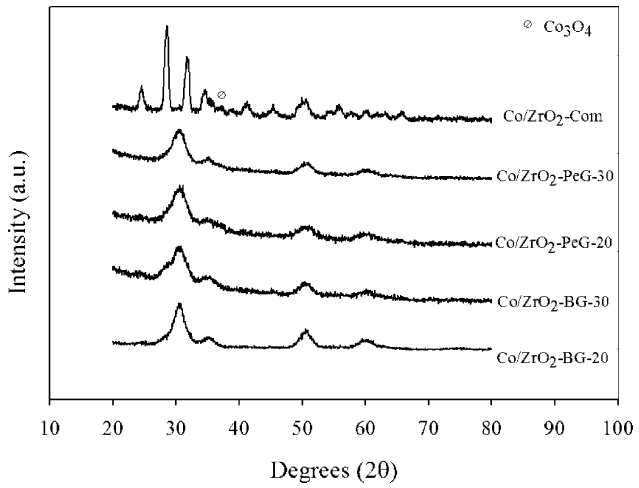

Fig. 3. X-ray diffraction patterns of various zirconia supported cobalt catalysts.

peaks tend to shift to lower temperatures. However, cobalt species supported on zirconia prepared in 1,5-pentanediol were found to be more difficult to reduce than the ones supported on zirconia prepared in 1,4-butanediol indicating a stronger metal-support interaction. The dotted line in the graph represents the standard reduction temperature used to reduce the catalysts prior to reaction (350 °C), it was found that on the zirconia prepared in 1,5-pentanediol and the commercial zirconia, a portion of cobalt oxide species could not be reduced at this temperature hence lower amount of active cobalt metals were available for H_2 chemisorption and CO hydrogenation reaction. Moreover, the selectivities for long chain hydrocarbons (C_{4+}) were found to be in the order: Co/ZrO_2–BG-20 > Co/ZrO_2–BG-30 > Co/ZrO_2–PeG-20 > Co/ZrO_2–PeG-30 > Co/ZrO_2-com. The unique properties of such glycothermal-derived zirconia supported cobalt catalysts offer interesting possibilities for catalyst design and applications.

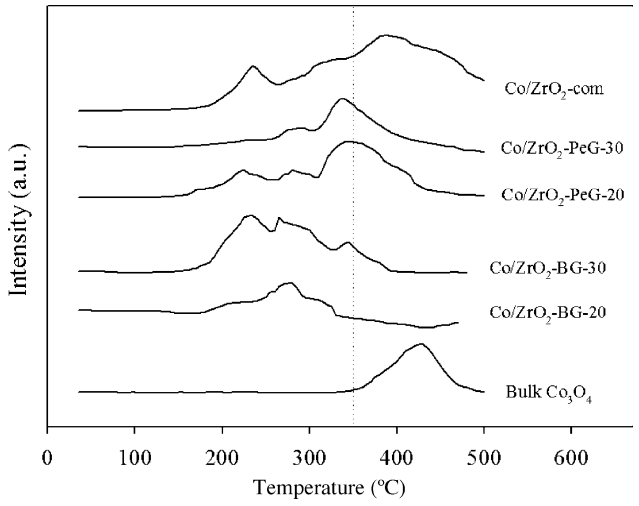

Fig. 4. Temperature programmed reduction (TPR) profiles of various zirconia supported cobalt catalysts.

4. Conclusions

Nanocrystalline zirconia prepared by the glycothermal method in two different glycols with various Zr content in the starting materials showed similar crystallite sizes of ca. 3–4 nm and large BET surface areas. Compared to commercial zirconia supported cobalt catalyst, the glycothermal-derived zirconia supported ones exhibited superior activities for CO hydrogenation with the use of zirconia prepared in 1,4-butanediol with lower amount of Zr content as the support resulted in the highest H_2 chemisorption and CO hydrogenation activities. The lower activities of cobalt catalysts supported on the zirconia prepared in 1,5-pentanediol were due to stronger interaction of cobalt and the zirconia supports as shown by higher reduction temperature peaks in the TPR profiles. The type of glycol used for preparation of the glycothermal-derived zirconia may affect the amount of crystal defects in the zirconia particles resulting in the difference in metal-support interaction behavior.

Acknowledgements

Financial supports by the Thailand Research Fund (TRF), TJTTP-JBIC, and the National Research Council of Thailand are gratefully acknowledged. The authors thank Dr. Nobuhiro Iwasa of the Graduate School of Engineering, Hokkaido University for BET measurements of the catalysts.

References

[1] Y. Nakano, T. Iizuka, H. Hattori, K. Tanabe, H. Hideshi, T. Kozo, J. Catal. 157 (1979) 1.
[2] K. Arata, K. Kato, K. Tanabe, Bull. Chem. Soc. Jpn. 49 (1976) 563.
[3] M. Inoue, H. Kominami, T. Inui, Appl. Catal. 97 (1993) 125.
[4] M. Inoue, H. Kominami, T. Inui, Catal. Lett. 65 (2000) 79.
[5] M. Inoue, Adv. Sci. Technol. 29 (2000) 855.
[6] E. Tani, M. Yoshimura, S. Somiya, J. Am. Ceram. Soc. 64 (1981) C-181.
[7] H. Nishisawa, N. Yamasaki, K. Matsuoka, J. Am. Ceram. Soc. 65 (1982) 343.
[8] G. Stefanic, S. Popovic, S. Music, Thermochim. Acta 303 (1997) 31.
[9] S. Kongwudthiti, P. Praserthdam, P.L. Silveston, M. Inoue, Ceram. Int. 29 (2003) 807.
[10] R.C. Reuel, C.H. Bartholomew, J. Catal. 85 (1984) 78.
[11] H.P. Klug, L.E. Alexander, X-ray Diffraction Procedures for Polycrystalline Amorphous Materials, 2nd ed., Wiley, New York, 1974.
[12] M. Kraum, M. Baerns, Appl. Catal. 186 (1999) 189.
[13] Y. Minato, K. Aoki, M. Shirai, M. Arai, Appl. Catal. A 209 (2001) 79.
[14] L. Ji, S. Tang, H.C. Zeng, J. Lin, K.L. Tan, Appl. Catal. A 207 (2001) 247.
[15] L. Guczi, Z. Schay, G. Stefler, F. Mizukami, J. Mol. Catal. A 141 (1999) 177.
[16] L. Guczi, L. Borko, Z. Schay, D. Basin, F. Mizukami, Catal. Today 65 (2001) 51.
[17] L. Guczi, G. Stefler, L. Borko, Z. Koppany, F. Mizukami, M. Toba, S. Niwa, Appl. Catal. A 246 (2003) 79.